Time-lapse by the numbers: elastic modeling of repeatability issues

David C. Henley, Joe Wong, and Peter M. Manning

ABSTRACT

An important emerging application for seismic reflection imaging is the remote monitoring of hydrocarbon production from a formation, or the injection of a fluid like CO_2 for sequestration underground. In this application, it is important for seismic data acquisition and processing to be reliably repeated at regular intervals, over a period of time sufficient to provide a 'difference anomaly' history of the monitored process. One way to explore the detectability of this anomaly is to model the time-lapse process numerically. Since elastic modeling is probably the most realistic way to simulate the earth response to a seismic survey, a state-of-the-art elastic modeling program was used to generate seismic surveys corresponding to several 'baseline' and corresponding 'time-lapse' 2D earth models. Each time-lapse model differed from its baseline only in a small subsurface zone, where properties were altered to simulate fluid exchange. This work explored the detectability of the time-lapse anomaly relative to various acquisition and processing parameters. With identical acquisition parameters for a baseline model and its matching time-lapse model, the detectability of the anomaly was surprisingly robust in the presence of both random and coherent noise. In the presence of significant simulated 'seasonal' statics variations, the anomaly remained detectable, with suitable processing. This study is a partial demonstration of the realistic modeling software available at CREWES, and the kinds of phenomena that can be usefully modeled.

INTRODUCTION

Time-lapse surveys

The fidelity of seismic reflection imaging has improved significantly over the last several decades, and in many cases, a survey image contains information about the fluids in place in the pore spaces of the rock layers. When this is the case, it may also be possible to detect subsequent changes in the fluid content of the rock pores, as during active production of an oilfield, for example. More recently, with increasing concern about the rising atmospheric concentration of CO_2, projects around the world have begun to demonstrate injection and sequestration of CO_2 into porous formations, often in conjunction with tertiary recovery of hydrocarbon fluids from those same formations. For both of these applications, it is useful to be able to monitor the progress of hydrocarbon production from, or CO_2 invasion into a porous layer, in order to optimize engineering decisions. The most straightforward approach is simply to design and execute a detailed seismic survey of the prospect before hydrocarbon production or CO_2 injection begins, then to repeat the survey at various time intervals in order to compare with the baseline survey and detect the changes in rock properties due to the production or injection activities.

Obviously, it is important to repeat the survey, and process its seismic data as exactly as possible, so that any changes can be attributed to rock property changes, not changes in the acquisition process, or differences in the processing flow. Insofar as possible, repeated seismic surveys should use either the same permanently installed sensors or, at least, the same sensor stations; and if possible, repeatable sources like Vibroseis should be deployed at the same source points. Even when the acquisition geometry is duplicated as closely as possible, variations in the near surface properties due to seasonal changes (water table variations, frozen surface in winter) can affect the repeatability of seismic surveys.

Complications in the earth itself which affect seismic imaging, and hence the detectable differences between various vintages of imaging along the same profile include significant near-surface weathering variations, as well as the velocity structure of the near surface. The latter can promote strong surface waves and weaker transmission of energy into the deeper subsurface for reflection imaging, while the former causes not only significant statics variations, but scattering of surface waves.

Elastic modeling

The numerical creation of synthetic seismic reflection data from known simple geological models has a long history of success in the seismic industry. For many applications, ray-trace modeling adequately simulates seismic data gathered either as vertical component data on land, or as an acoustic component in the marine environment. For our study of time-lapse detection, however, we wished to generate realistic data sets, including all elastic wave phenomena, like ground roll and scattering, that would be detected by surface sensors. Hence, we chose to use the elastic wave modeling software created by Peter Manning (Manning, 2008, 2009, 2010a, 2010b, 2011a, 2011b.). The specific algorithm used is a MATLAB application called mFD2D, modified by Joe Wong from research code written by Manning (Wong et al, 2012).

In collaboration with Manning, Wong created a series of paired simple earth models in the file format required by the modeling program. Each pair of models consisted of a 'baseline' model and a 'time-lapse' model, in which a designated target zone contained elastic parameters modified slightly from those in the baseline model to create a time-lapse 'anomaly'. Wong, in consultation with Henley, chose suitable acquisition geometry for surveying all the models, and created sets of seismic source gathers, in SEGY format, corresponding to the various pairs of baseline and time-lapse models.

To simulate the conditions for processing sets of actual field data, the SEGY files were processed in ProMAX by Henley, with *no prior knowledge* of the input model parameters. In this way, parameters for coherent noise attenuation, NMO correction, and statics correction were *determined from the data*, not from known model parameters, thus more realistically emulating field data.

METHODS

Routine processing

For this study, we elected to process the data just as we would the data for any seismic survey, omitting only the application of elevation and/or refraction statics. Our objective was to see how detectable the time-lapse anomaly was after more or less 'routine' processing, at the level of the 'static-corrected stack'. Hence we analyzed raw source gathers to estimate parameters for coherent noise attenuation using radial trace (RT) filters on the baseline study in each case (Henley, 2011), then applied the filters to both baseline and time-lapse models for each instance. Pre-stack deconvolution was applied using Gabor deconvolution (Margrave et al, 2011), although the wavelet (whose spectral characteristics were established by parameter selection in the software) applied in the elastic modeling was not appreciably whitened during the deconvolution. NMO velocities were determined by visually fitting hyperbolae to visible events on source gathers on the baseline survey of each pair, then applied to both baseline and monitor surveys of each pair. Residual statics were determined using the maximum-stack-power autostatics algorithm in ProMAX (Ronen and Claerbout, 1985), where we had the option to derive and apply statics on the baseline survey, then to apply them to both surveys, or to run the program on each survey independently. After application of the autostatics to NMO-corrected source gathers, the CMP stacks were formed; post-stack deconvolution (Gabor decon), and FX deconvolution (for random noise attenuation) were applied to improve resolution in both dimensions. For this study, we used only the vertical component data created by the elastic modeling program; the radial component data await similar future studies.

Novel processing

As an alternative to autostatics, we decided to test raypath interferometry (Henley, 2012a) since the algorithm is less sensitive to individual statics variations than autostatics methods. While far more computation-intensive than standard autostatics methods, raypath interferometry requires no time adjustment of the final time-lapse stack to match the baseline stack, as can be necessary with independent autostatics solutions.

While not strictly ‘novel’ processing, the comparison methods used to highlight the differences between time-lapse and baseline models formed a part of the experimental process. We tested simple subtraction of stacks, least-squares subtraction of stacks, and the stack of subtracted source gathers, both with and without post-stack migration. Our future plans include applying the matched filter approach described by Al-Mutlaq and Margrave (2011, 2012) on these models as well.

RESULTS

The model geometry

Figure 1 shows a simple layer model, 2000m x 1000m, used as input to the elastic modeling program. The only notable feature in this model is a gently undulating near-surface interface simulating the base of weathering. Figure 2 shows the corresponding time-lapse model, where a 400m long zone in the centre of the model has a velocity 10% less than the material flanking it in the same zone. This anomaly is larger, stronger, and nearer the surface (and hence more detectable) than many anomalies likely to be of interest in industry, but a strong anomaly allows us to better test repeatability effects in acquisition and processing than a faint one. Both models were surveyed using a receiver interval of 2m, and a source interval of 10m, where the source was moved through the fixed receiver spread. This acquisition geometry was used for all subsequent models. To test lateral resolution issues and coherent noise attenuation, each original survey could be readily modified to simulate 10m receiver spacing, simply by applying a 5-trace mixing operation to the original source gathers, then selecting every 5^{th} trace of the mixed gathers as the output of a 5-receiver array.

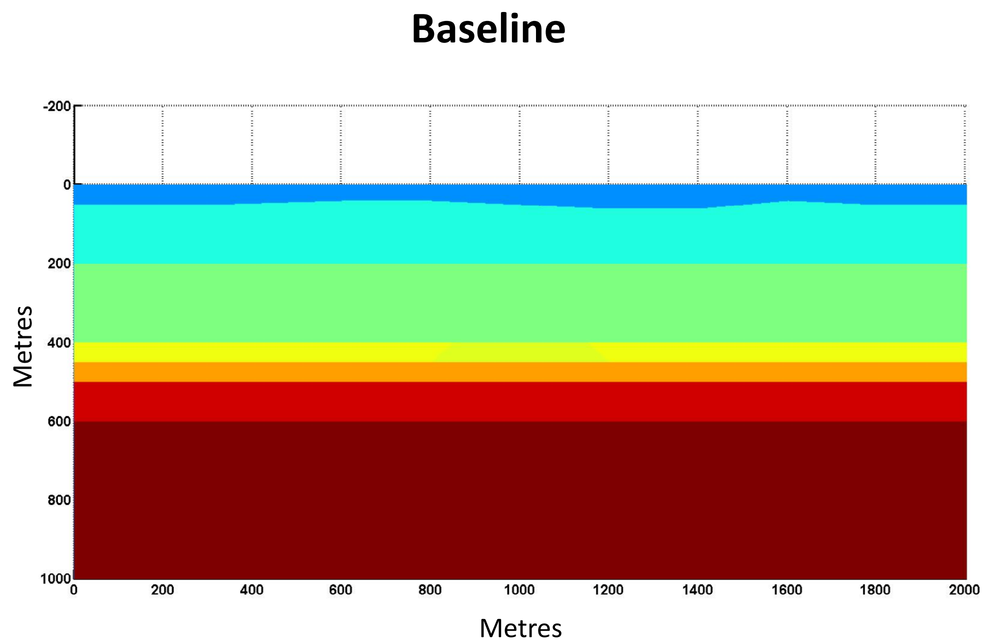

FIG.1. Example of a simple model used in elastic modeling to create seismic data for a baseline survey.

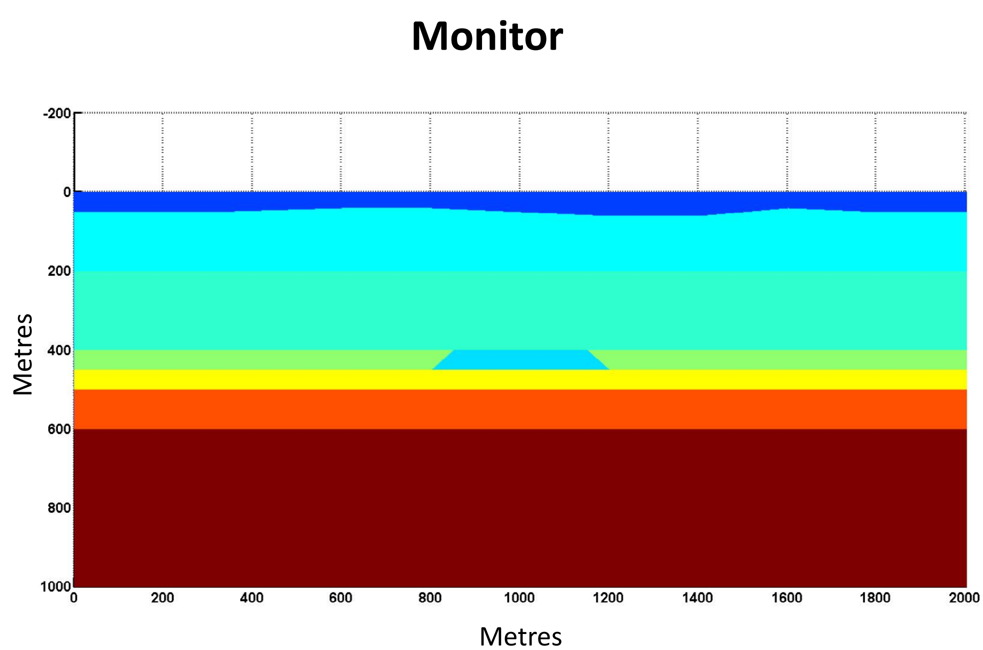

FIG.2. Model from Figure 1 after the insertion of a time-lapse anomaly within one layer. The anomaly is 50m x 400m and constitutes a 10% velocity decrease.

Simple model results

Not surprisingly, the brute CMP stacks of the vertical components of these two models, shown in Figures 3 and 4, show the model details quite clearly, with multiples and computation artifacts visible on both sections beneath the deepest reflection events. The base of weathering interface is imaged quite well, and we see a slight sag in deeper events beneath the valley in this interface. The time-lapse anomaly in Figure 4 is easily visible, as well, comprising a dimming of the 300ms event, corresponding brightening of the 350ms event, and increased time sag on the deepest event. These models have no statics, so the stacks can be simply subtracted, with no relative time shift; and the results of such a subtraction are shown in Figure 5. As we expect, the time-lapse anomaly is by far the most prominent feature on this section, showing both top and bottom events, as well as edge diffractions. The deeper event at 425ms is also prominent due to its anomaly-induced time sag, causing a timing mismatch with the corresponding event on the baseline section. Note that the time-sag anomaly persists well beyond the edges of the actual time-lapse amplitude anomaly, due to the oblique transmission of energy through the actual anomaly on source gather traces at longer offsets. If we migrate the image in Figure 4, the result is Figure 6, where the migration operator has eliminated the diffractions, but the lateral extent of the anomaly is not decreased, nor are the edges sharpened. Likewise, if we migrate the difference image in Figure 5, the diffractions disappear, but the resolution of the anomaly is basically unchanged (Figure 7).

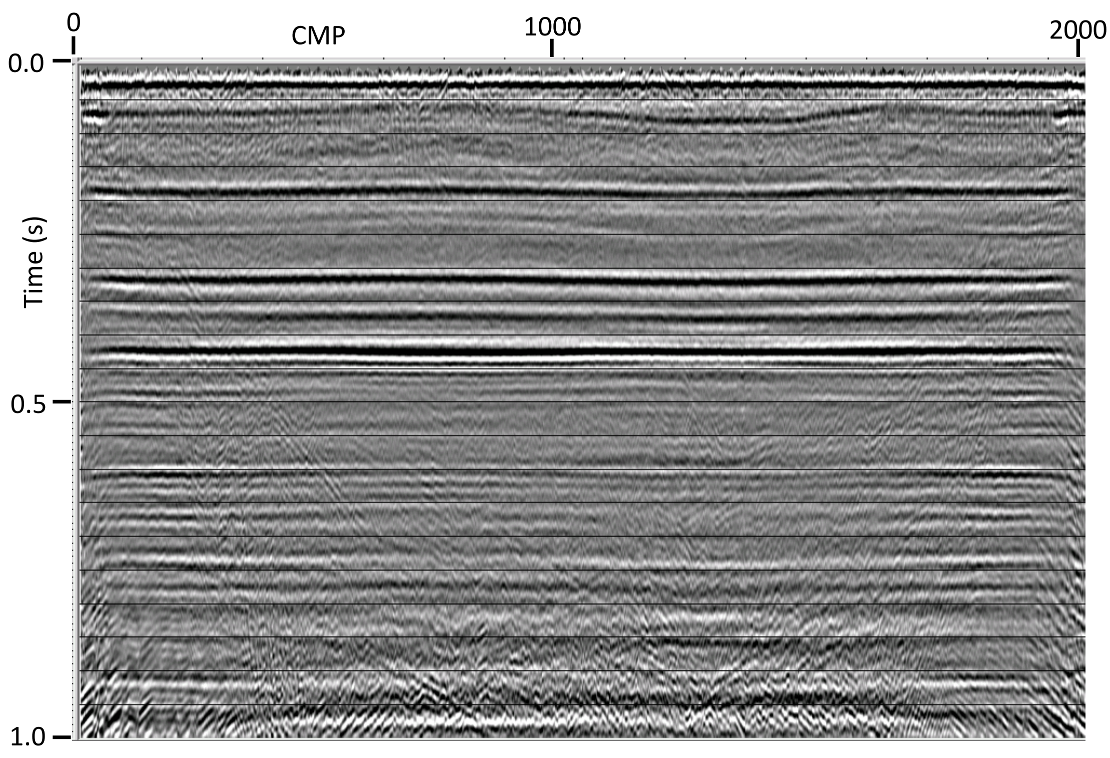

FIG.3. Brute CMP stack of the vertical component seismic data created by 2D elastic modeling algorithm from the model description in Figure 1. This is the 'baseline' model.

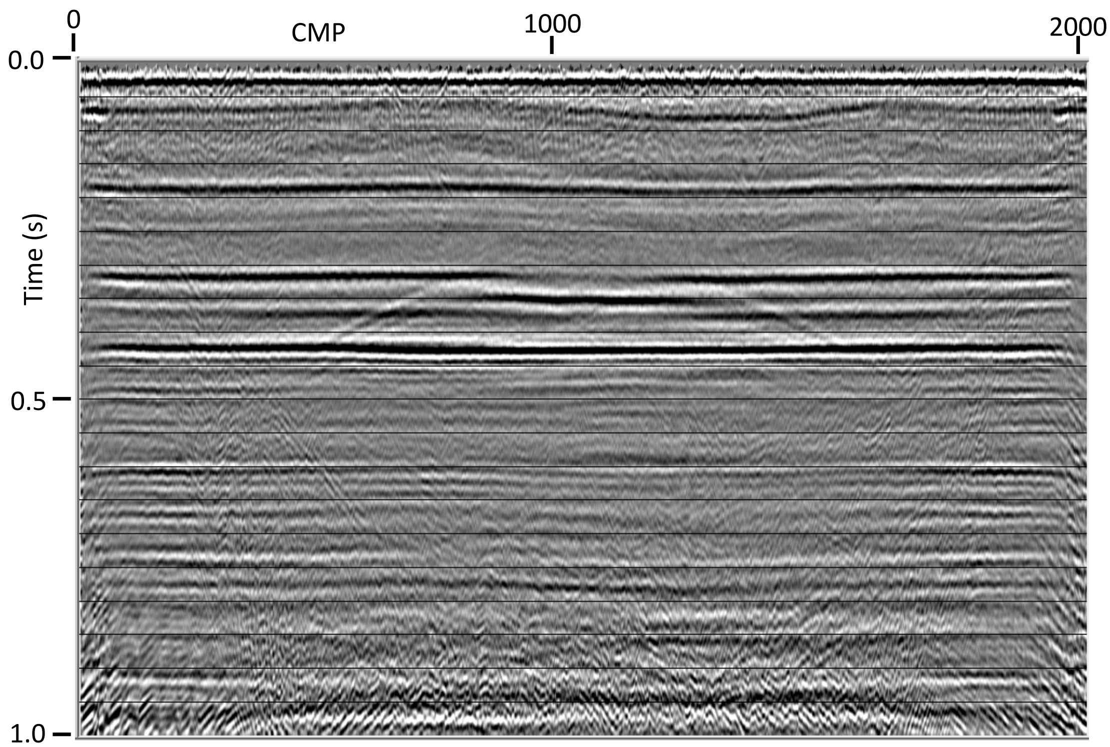

FIG.4. Brute CMP stack of the vertical component seismic data created by 2D elastic modeling algorithm from the model description in Figure 2. This is the ‘monitor’ model.

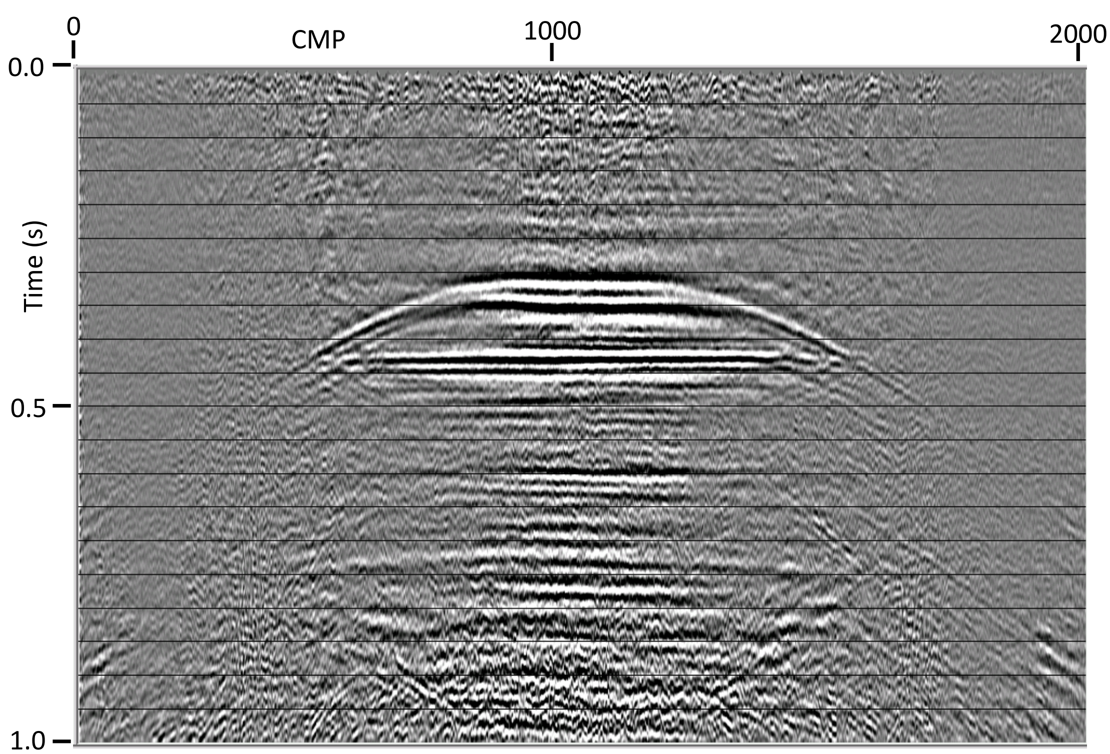

FIG.5. Arithmetic difference between the ‘monitor’ and ‘baseline’ stacks in Figures 3 and 4.

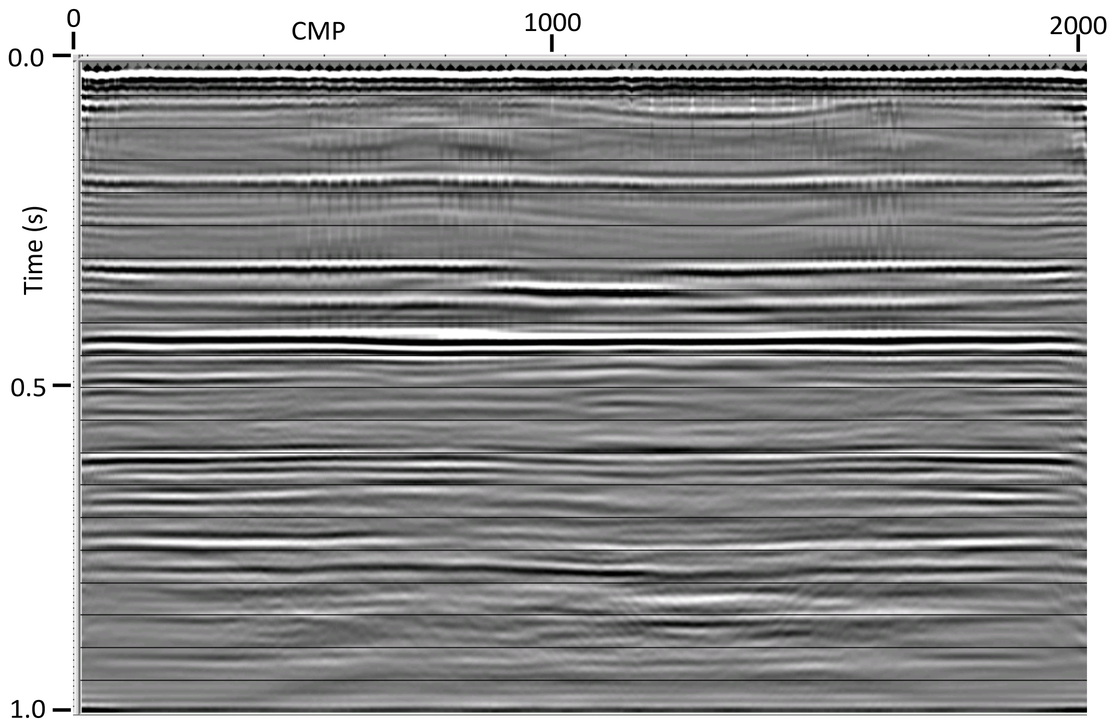

FIG.6. Post-stack migrated version of the stack in Figure 4. The diffractions from the edges of the anomalous zone have vanished, but the anomaly is not better resolved.

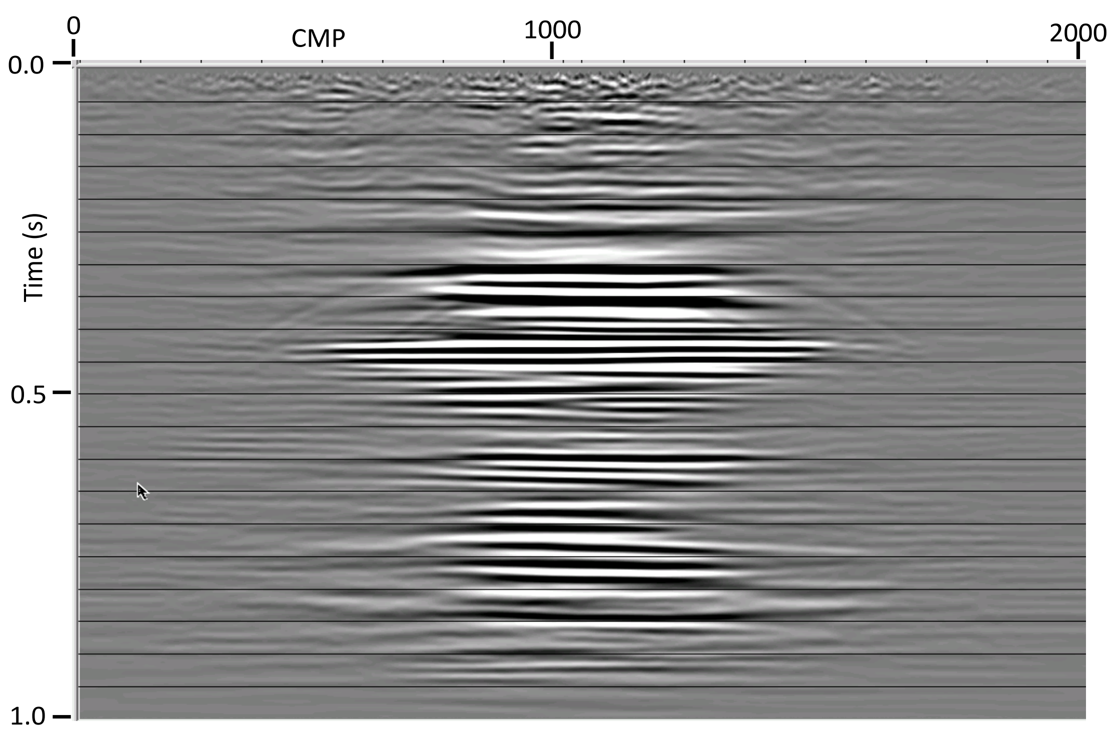

FIG.7. Migrated version of difference image in Figure 5. Diffractions are largely gone, but lateral resolution is not appreciably increased.

The pair of simple surveys was also compared by subtracting their individual source gathers, then stacking the 'difference' gathers. As the result in Figure 8 shows, the anomaly looks much the same as in Figure 5, but more noise survives on both sides of the anomaly (both this display and the ones in Figures 5 and 7 were normalized for the entire display, rather than by individual traces.

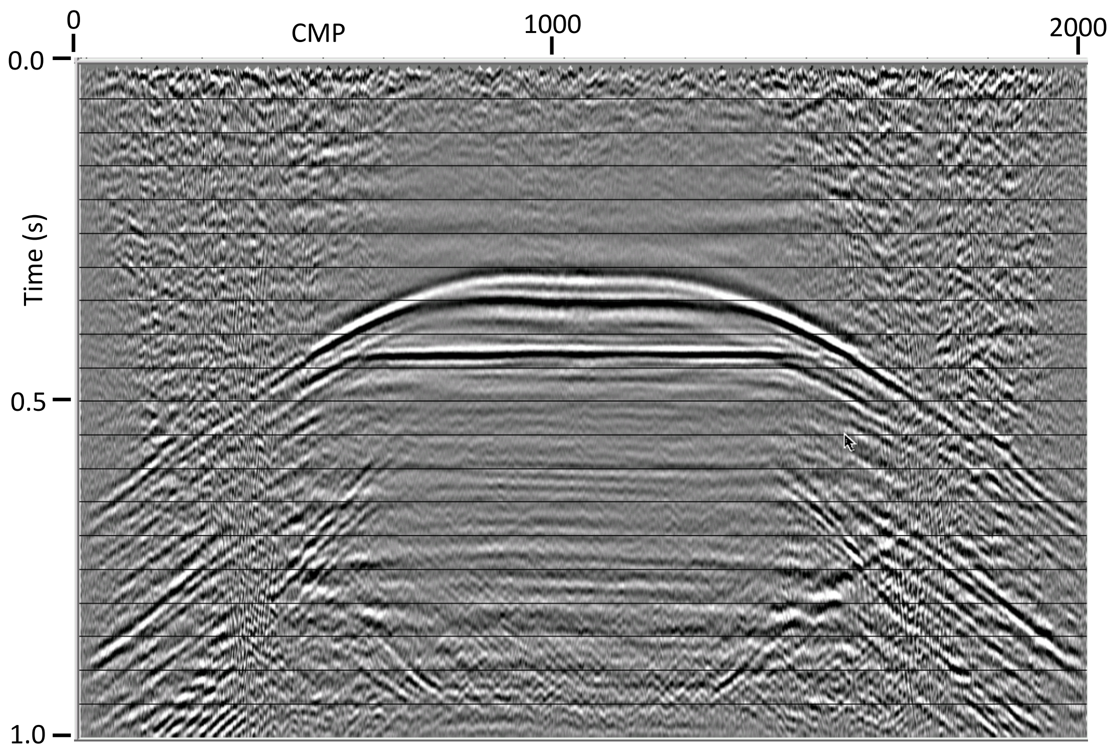

FIG.8. Brute CMP stack of the 'difference' shot gathers from the 'baseline' and 'monitor' surveys, created by subtracting all corresponding shot gathers from the two surveys.

Since the elastic modeling program itself provides perfectly clean data, we externally created bandlimited random noise and added it to the source gathers from both the baseline and time-lapse surveys. We added an unrealistically large amount of noise (S/N = 0.5), making the reflections difficult to detect on the raw records. The stack image of the baseline survey with this added noise is shown in Figure 9. Clearly, all the legitimate reflections survived, although their bandwidth appears reduced from that of the no-noise reflections in Figure 3. Interestingly, the computational artifacts and multiples are no longer visible. The comparable display for the time-lapse survey comprises Figure 10, on which the anomaly is still clearly visible. The image in Figure 11, the result of subtracting the stacks in Figures 9 and 10, is surprising, not only because it clearly shows the anomaly, but because the actual physical size of the anomaly is better portrayed in this image than in any of the other images in Figures 5, 6, and 7.

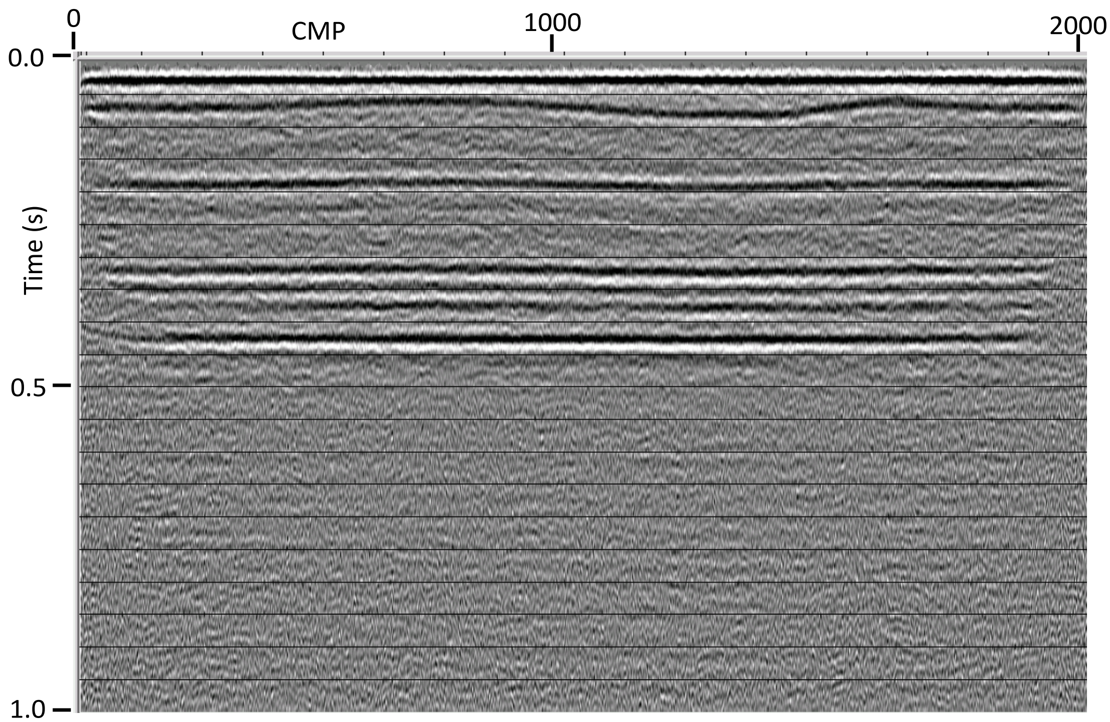

FIG.9. Brute CMP stack of vertical component seismic data from 2D elastic modeling of the model in Figure 1, but with bandlimited random noise added to the traces, S/N = 0.5 (very strong noise).

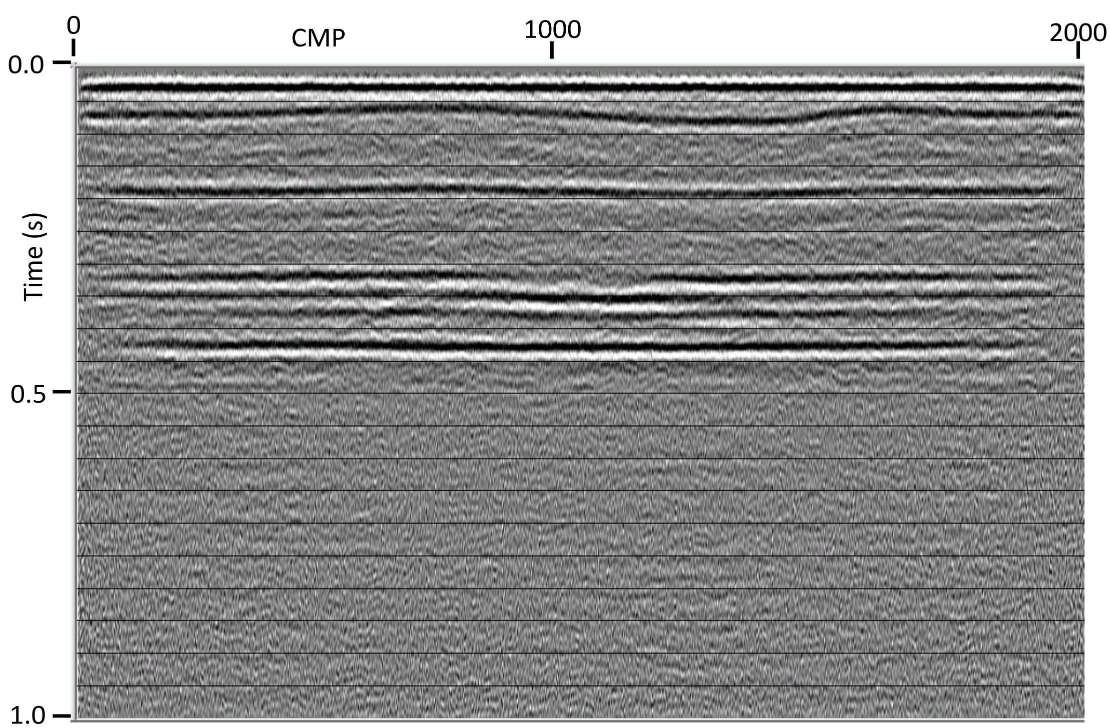

FIG.10. Brute CMP stack of vertical component seismic data from 2D elastic modeling of the model in Figure 2, but with bandlimited random noise added to the traces, S/N = 0.5.

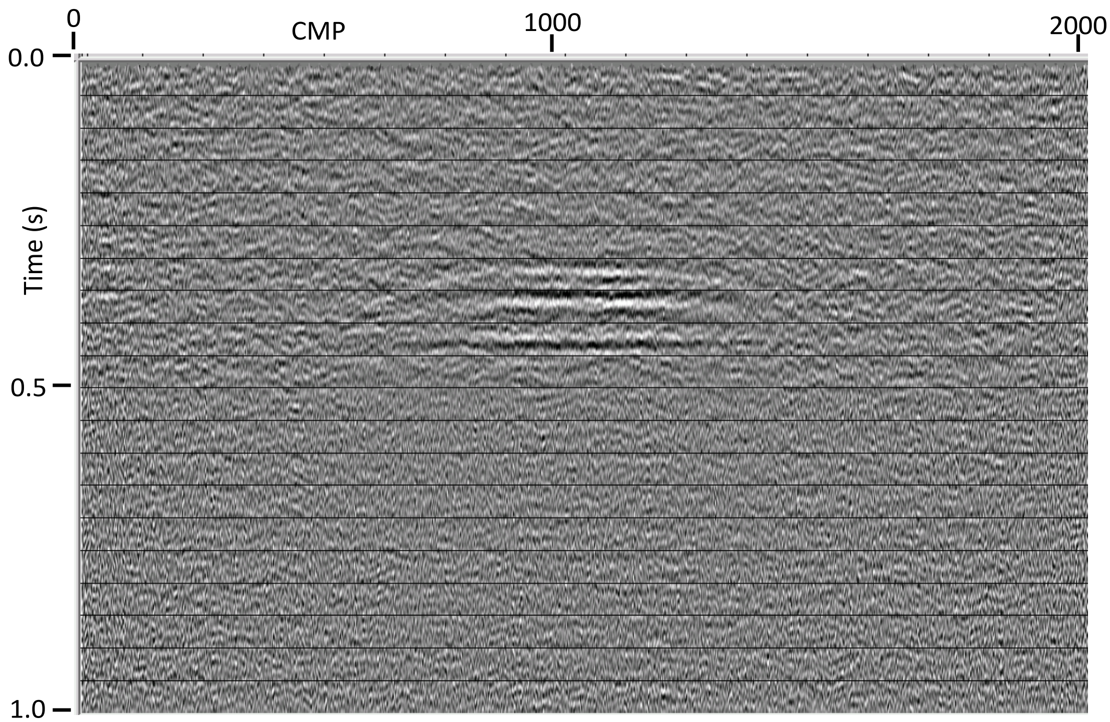

FIG.11. Difference of the brute stacks shown in Figures 9 and 10. Even in the presence of very strong random noise, the time-lapse anomaly is visible, as long as acquisition geometry is identical for the two surveys, and there are no statics.

To test the importance of the 2m receiver spacing for resolving the lateral extent of the anomaly, we created data sets, for both the baseline and time-lapse surveys, which simulated 10m receiver spacing, by trace mixing and decimation of the original source gathers. The corresponding stacks and stack difference are displayed in Figures 12, 13, and 14, respectively. While the images in these figures appear somewhat more blurred laterally, relative to Figures 3, 4, and 5, it appears that 10m spatial sampling is totally adequate for detecting the time-lapse anomaly and estimating its dimensions.

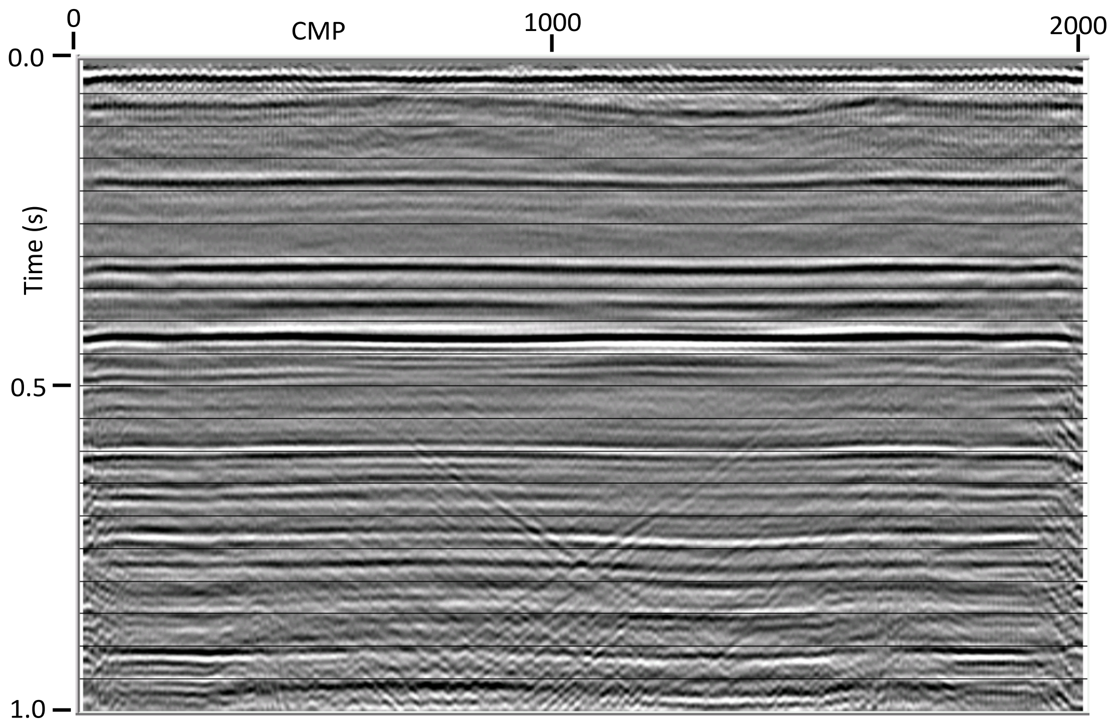

FIG.12. Brute CMP stack of vertical component data from 2D elastic modeling of the ‘baseline’ model in Figure 1, but using simulated receiver spacing 10m, rather than 2m. Lateral resolution is reduced, and somewhat more coherent noise survives. There is no additive noise.

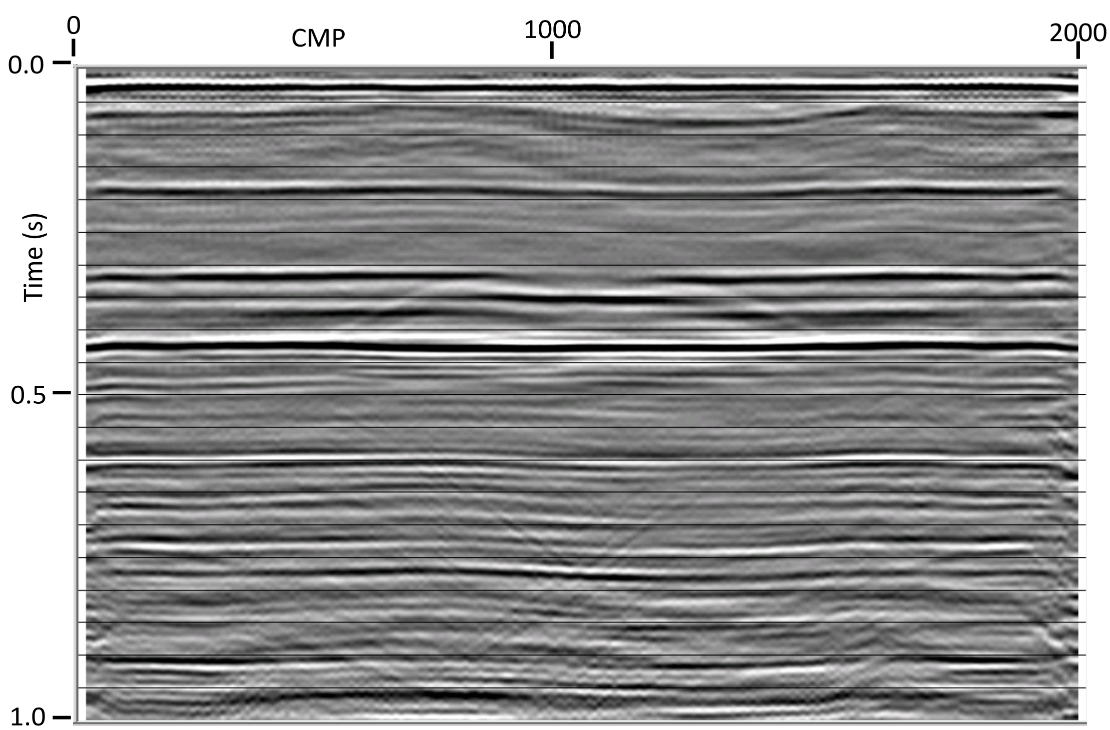

FIG.13. Brute CMP stack of vertical component data from 2D elastic modeling of the ‘monitor’ model in Figure 2, using simulated receiver spacing 10m, rather than 2m. No additive noise.

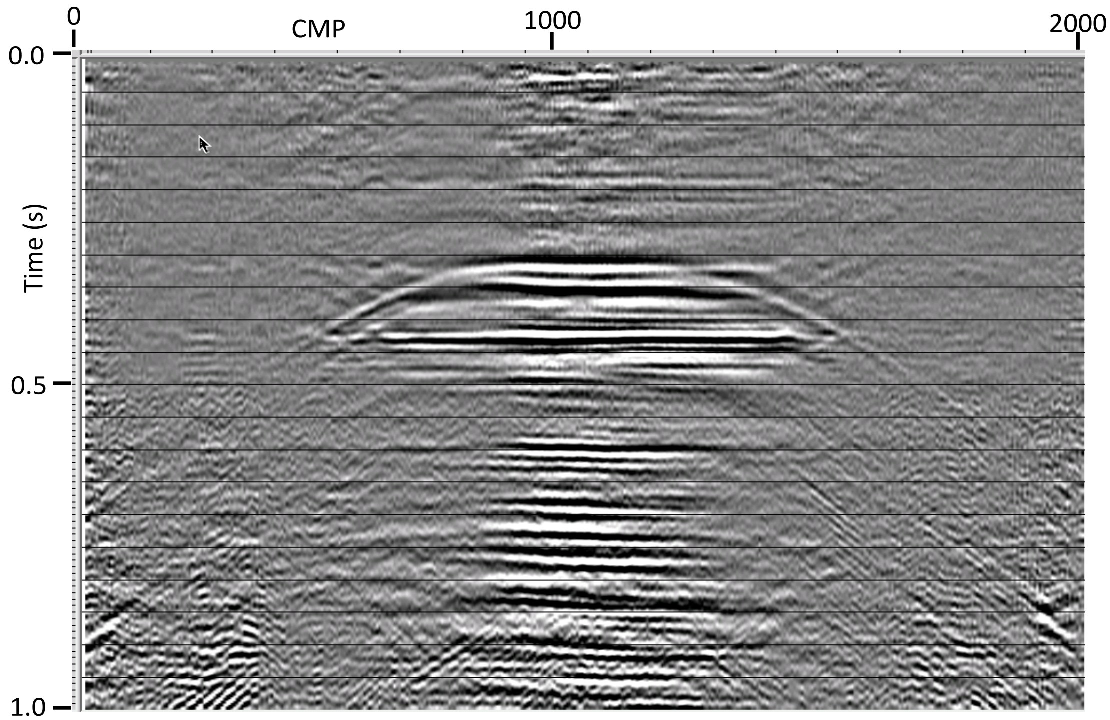

FIG.14. Difference of the two brute stacks in Figures 12 and 13. Comparing with Figure 5, we conclude that 10m receiver spacing would be entirely adequate for monitoring this time-lapse survey, when acquisition parameters are unchanging, and there is little additive random noise.

More complex models

Our comparison of a pair of simple models allowed us to evaluate a few processing parameters and techniques for comparing time-lapse data with corresponding baseline surveys. In the real world, however, two of the most troublesome aspects of land seismic data are likely to greatly affect the detectability of time-varying subsurface anomalies. Both of these problems are created by the near surface: coherent, source-generated noise, and varying time delays, or statics, for reflection events recorded on the surface. The strength and bandwidth of surface waves and near-surface guided waves is controlled primarily by the overall layer thickness and velocity contrast at near-surface boundaries, while static delays are created by variations in the thickness and velocity of the weathered layer itself. The same surface variations that cause static shifts can also act as scattering centres for surface waves, thus compounding the problem. To create a pair of model seismic surveys that would more realistically incorporate some of these effects, Wong modified the near-surface layer so that it had much lower velocity, but also so that the surface layer itself contained pockets of even lower velocity. Figure 15 shows the new, more complex baseline model, while Figure 16 features the corresponding time-lapse model. Although the added complexity does not, at first glance, appear to be very large, its influence on the seismic records created by the modeling package is profound. Figure 17 shows a vertical component source gather from the earlier simple baseline model in Figure 1, while Figure 18 shows the vertical component source gather at the same source point from the more complex model in Figure 15. Due to the strong surface-wave noise, and scattered surface waves from surface static anomalies, the underlying reflections are no longer visible on raw source gathers.

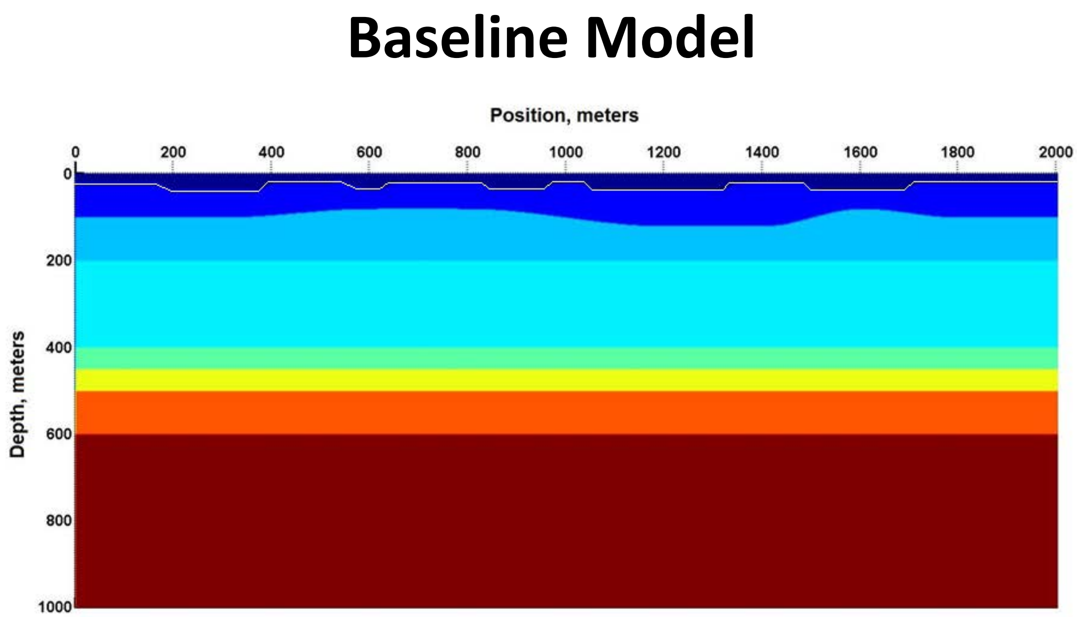

FIG.15. Same model as Figure 1, except near-surface layer has a stronger velocity contrast with the underlying layers, and there are several 'weathering' anomalies at the surface.

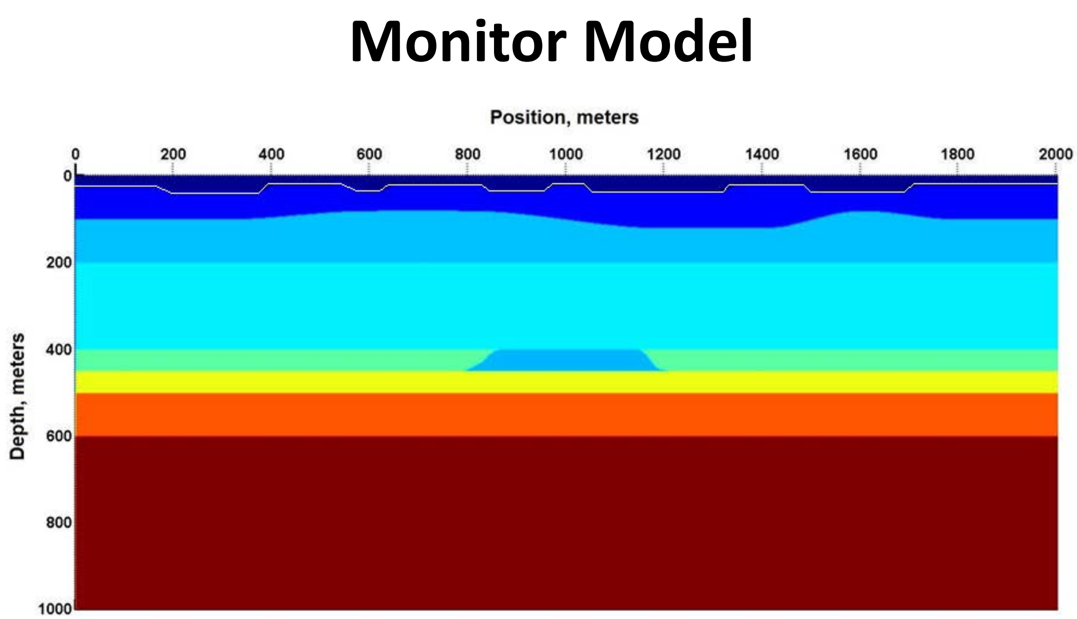

FIG.16. Same model as Figure 2, except near-surface layer has a stronger velocity contrast with the underlying layers, and there are several 'weathering' anomalies at the surface.

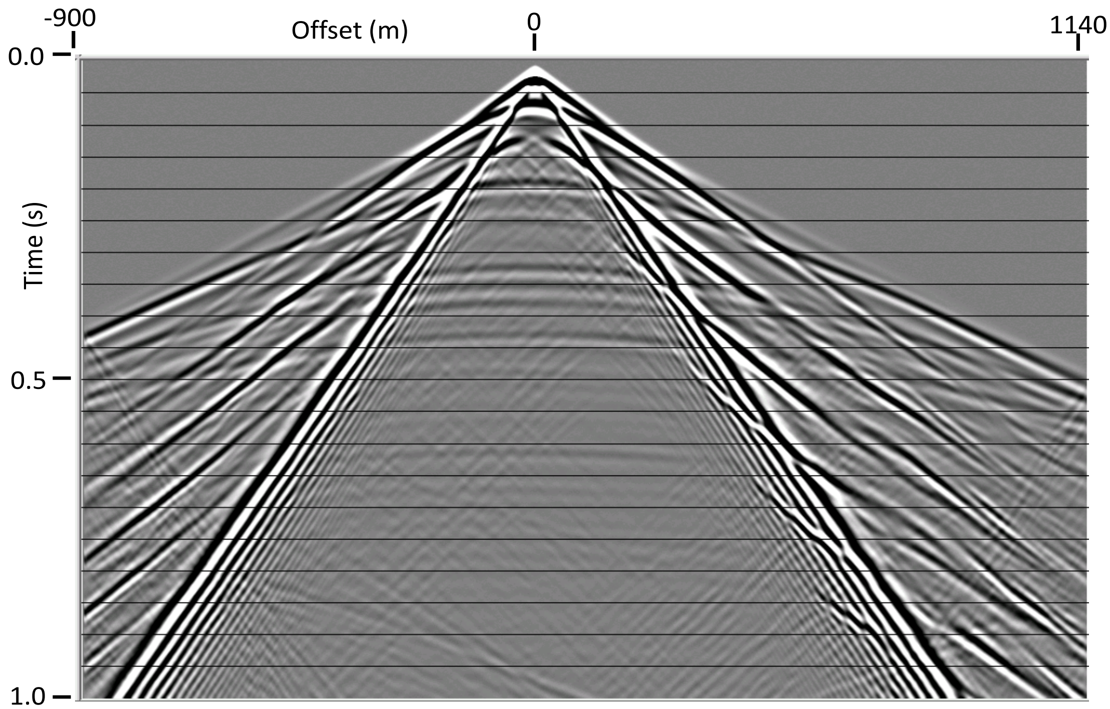

FIG.17. Typical vertical component source gather from the model in Figure 1, with no weathering anomalies, larger velocity contrast between surface layer and underlying layers. Strong coherent noise results.

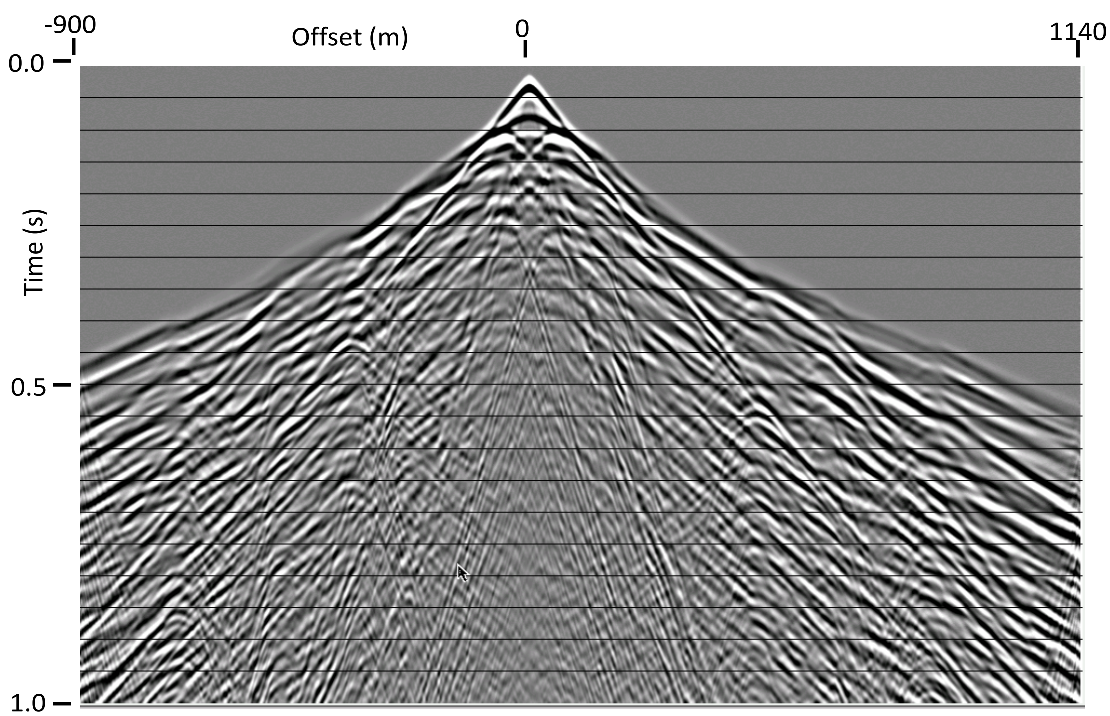

FIG.18. Typical vertical component source gather from the model in Figure 15, where strong near-surface velocity contrasts cause strong coherent noise, and weathering anomalies cause noise scattering.

After the application of several RT filter passes and Gabor deconvolution, the source gather in Figure 18 is displayed again in Figure 19. The long-offset limbs of some reflections can now be seen (and used to determine NMO velocities for stacking). After all source gathers were RT filtered and deconvolved, the brute CMP stack (no statics applied) was formed (Figure 20). Note that although the undulating ‘base of weathering’ horizon can be clearly seen, the unresolved statics seriously degrade the imaging of all horizons. The brute CMP stack of the time-lapse model, in Figure 21 fares no better, and in fact, the time-lapse anomaly is not detectable on the stack alone, as it was for the simple model.

After applying three separate passes of maximum-stack-power autostatics, the stack is improved considerably, as shown in Figure 22. Figure 23 shows that the same thing happens for the time-lapse stack, when the same autostatics passes are applied (using the same parameters as for the baseline model). The time-lapse anomaly is now visible as a dimming of the 350ms event, but is comparable to other amplitude variations on this section. Subtracting the stacks in Figures 22 and 23, we obtain the difference image in Figure 24. It should be noted, however, that a bulk shift of 6ms was required to properly align these sections before subtraction, due to the slightly different statics generated by the separate runs of the autostatics program on the individual models.

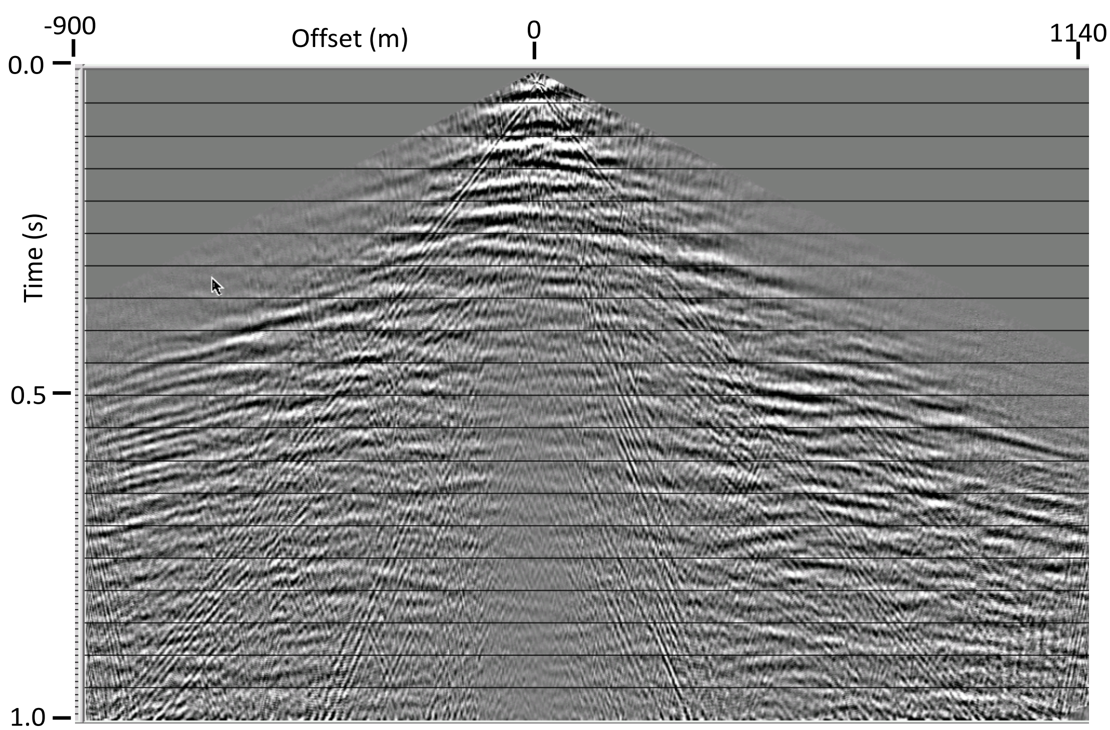

FIG.19. Vertical component source gather in Figure 18 after application of RT filtering and Gabor deconvolution. Some reflections are now visible at longer offsets.

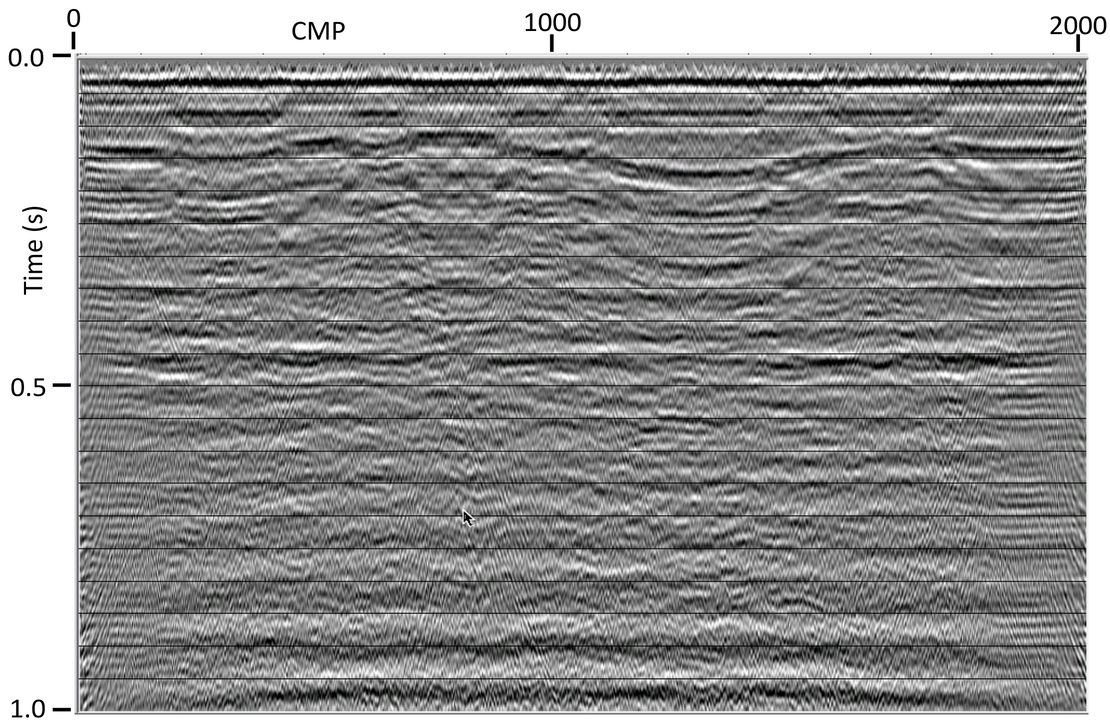

FIG.20. Brute CMP stack of source gathers for the baseline model in Figure 15, after RT noise attenuation and Gabor deconvolution. No statics have been applied.

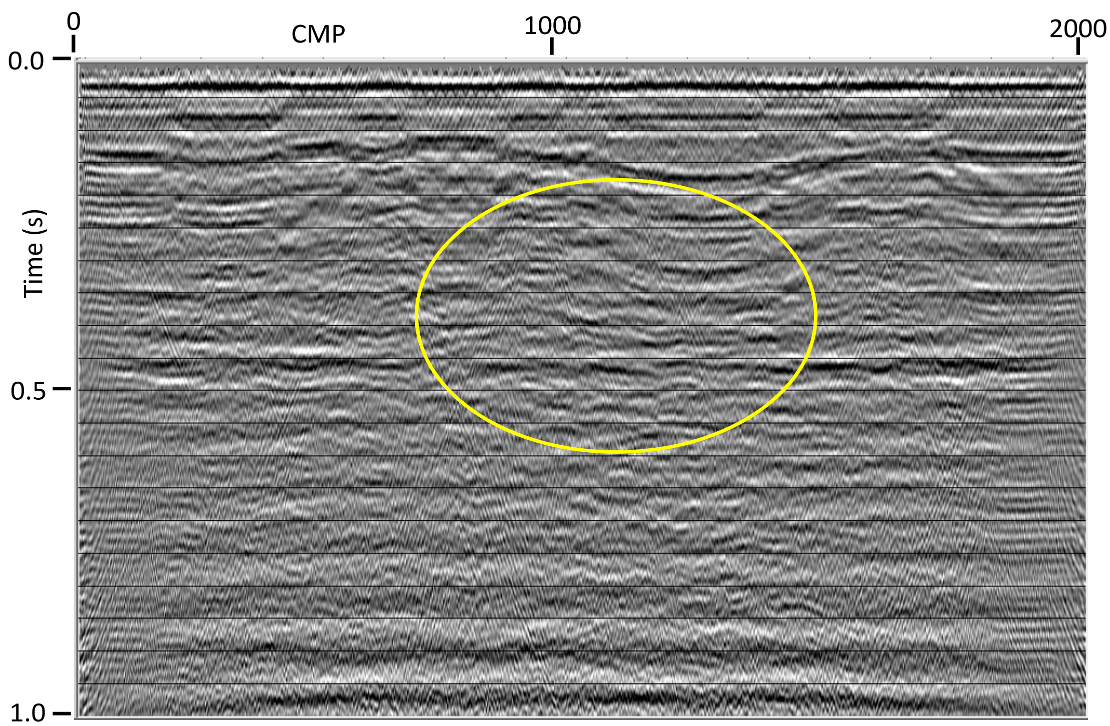

FIG.21. Brute CMP stack of source gathers from the model in Figure 16, after RT filtering and Gabor deconvolution. The time-lapse anomaly can't be reliably seen when comparing with Figure 20.

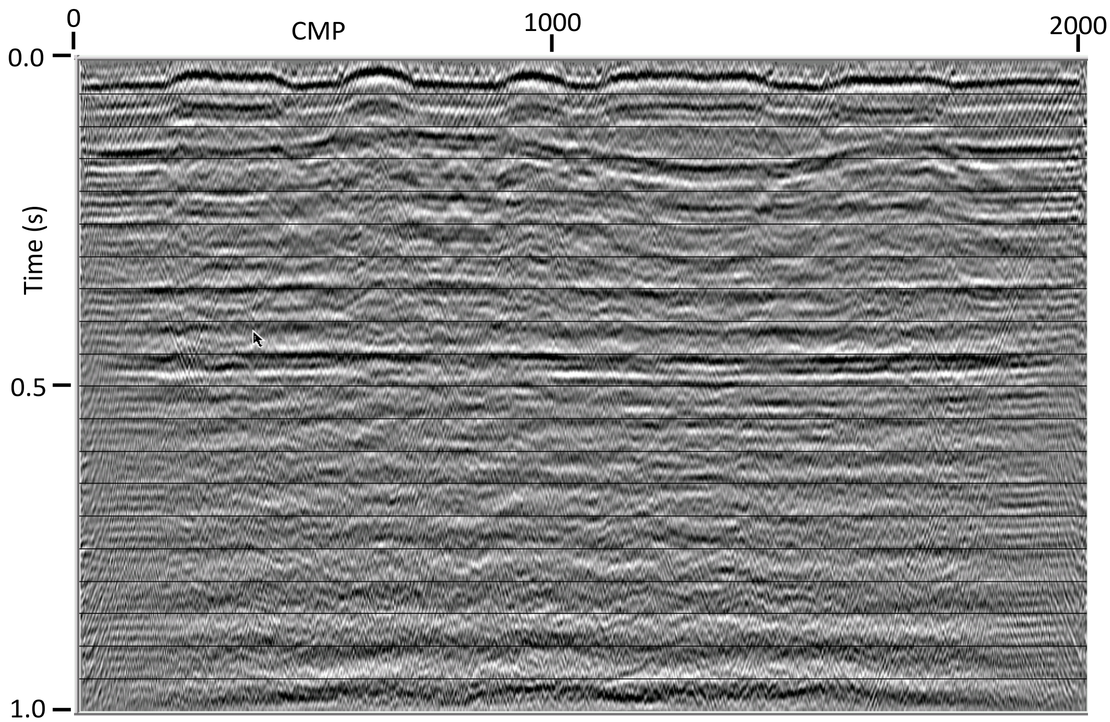

FIG.22. Stacked vertical component seismic data from ‘baseline’ model in Figure 15 after three passes of autostatics. All reflection events show more continuity than in Figure 20.

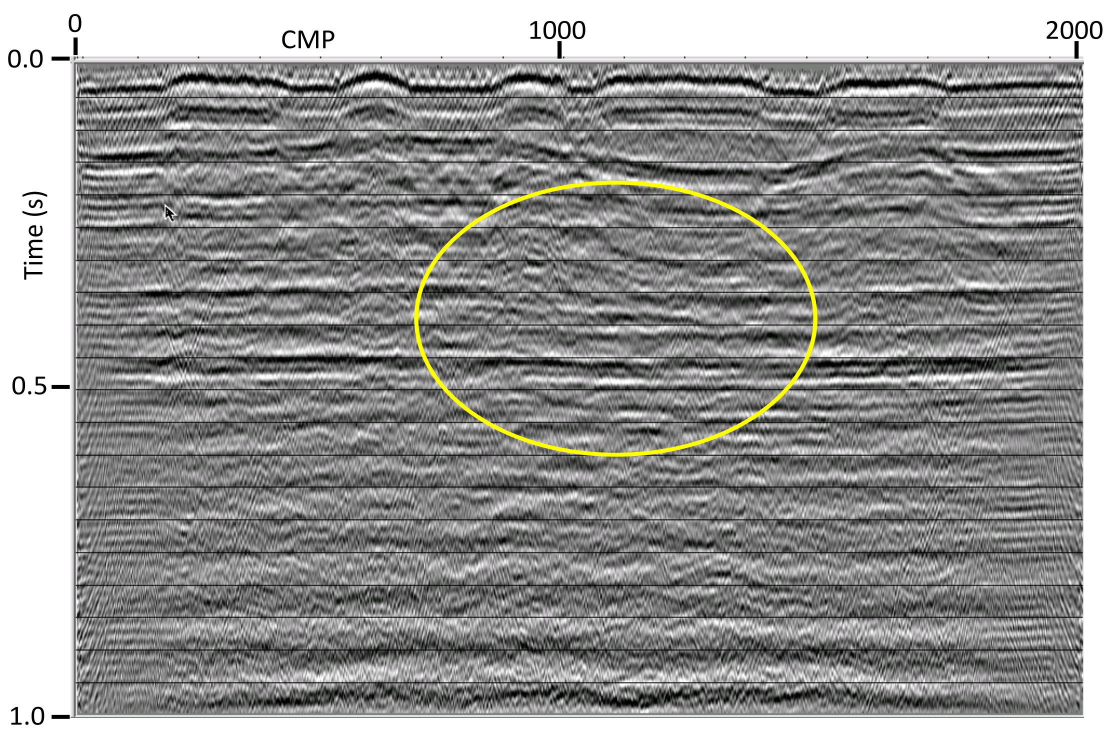

FIG.23. Stacked vertical component seismic data from ‘monitor’ model in Figure 16 after three passes of autostatics, using the same parameters as for the ‘baseline’ image. The anomaly is barely detectable.

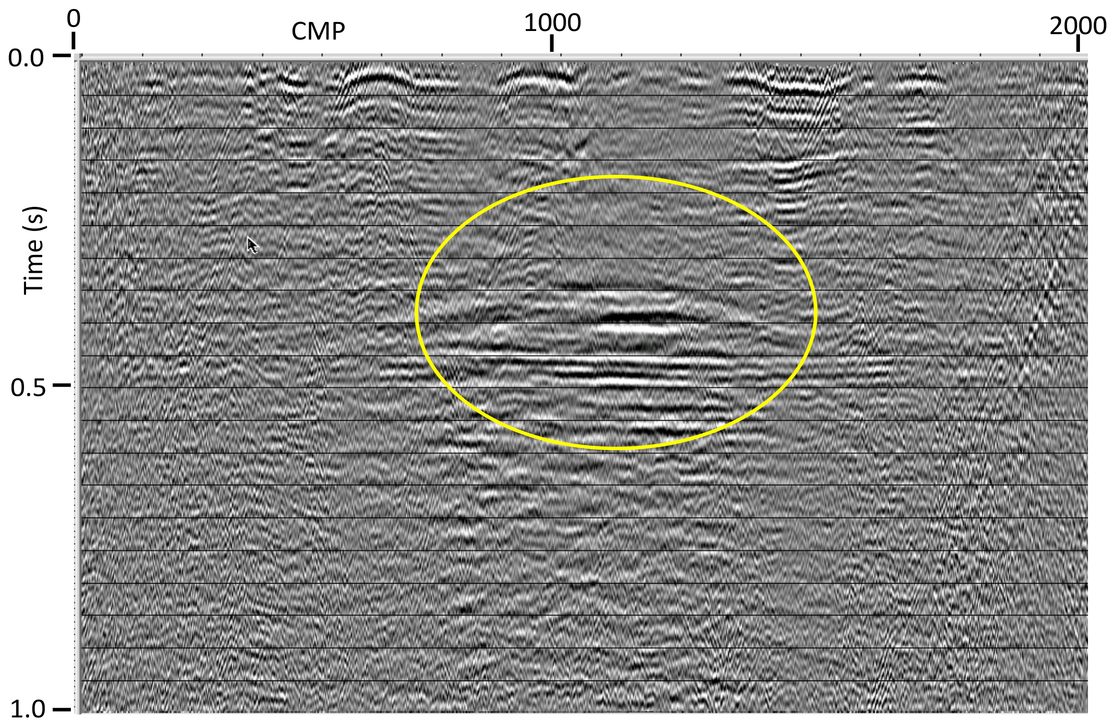

FIG.24. Difference between the images in Figures 22 and 23. Time-lapse anomaly is clearly visible. Relatively large image differences near the surface are likely due to actual differences in the autostatics solutions, in spite of the use of identical parameters for both 'baseline' and 'monitor' surveys.

To increase the anomaly-detection difficulties further, we added bandlimited random noise to the source gathers for both the baseline and time-lapse models, with S/N = 1.0. The corresponding brute CMP stacks are shown in Figures 25 and 26, and the static-corrected stacks in Figures 27 and 28. The noise surviving the stack diminishes the amplitudes of the reflections enough that the time-lapse anomaly can only barely be seen on the static-corrected stack. Indeed, as shown in Figure 29, while the anomaly can be seen on the stack difference, its amplitude is now less than some of the near-surface differences, and the top of the anomaly, at 350ms is not visible at all. However, if the *identical* autostatics solutions (from the baseline survey) are applied to the data from both surveys, the near-surface differences vanish, leaving only the actual time-lapse anomaly, although still very faint, and not visible at its 350ms inception time (Figure 30).

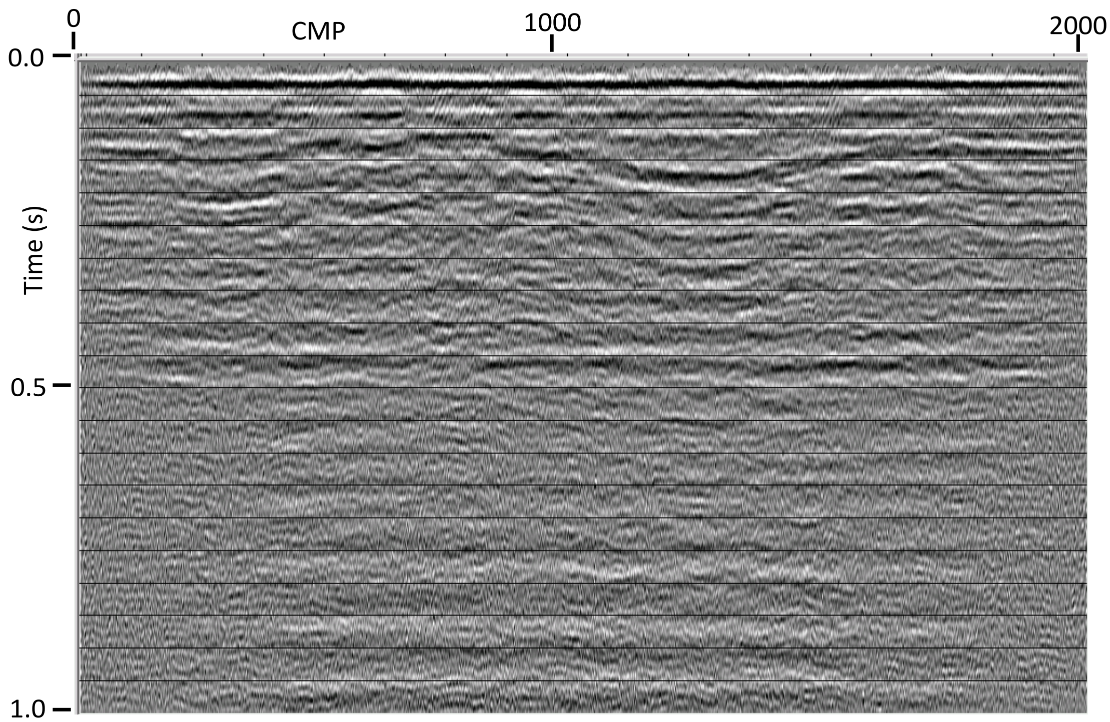

FIG.25. Brute CMP stack of vertical component data from ‘baseline’ model in Figure 15 with bandlimited random noise added to the seismic data (S/N = 1.0). No statics have been applied.

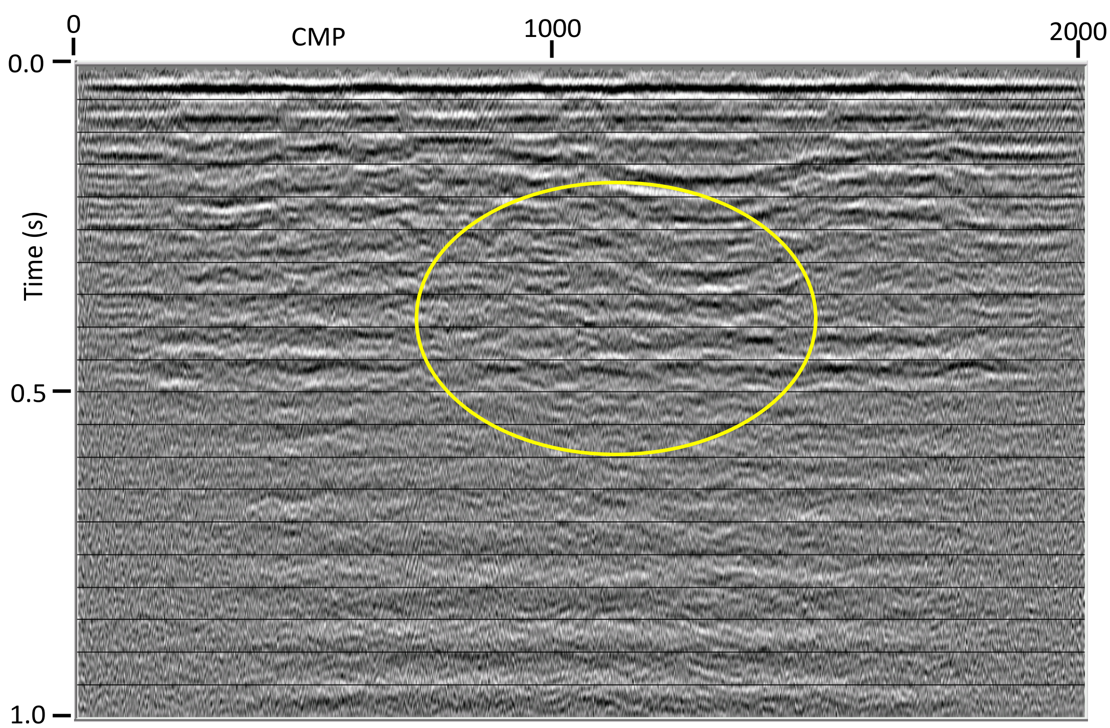

FIG.26. Brute CMP stack of vertical component data from ‘monitor’ model in Figure 16 with bandlimited random noise added to the seismic data (S/N = 1.0). Anomaly is impossible to see reliably.

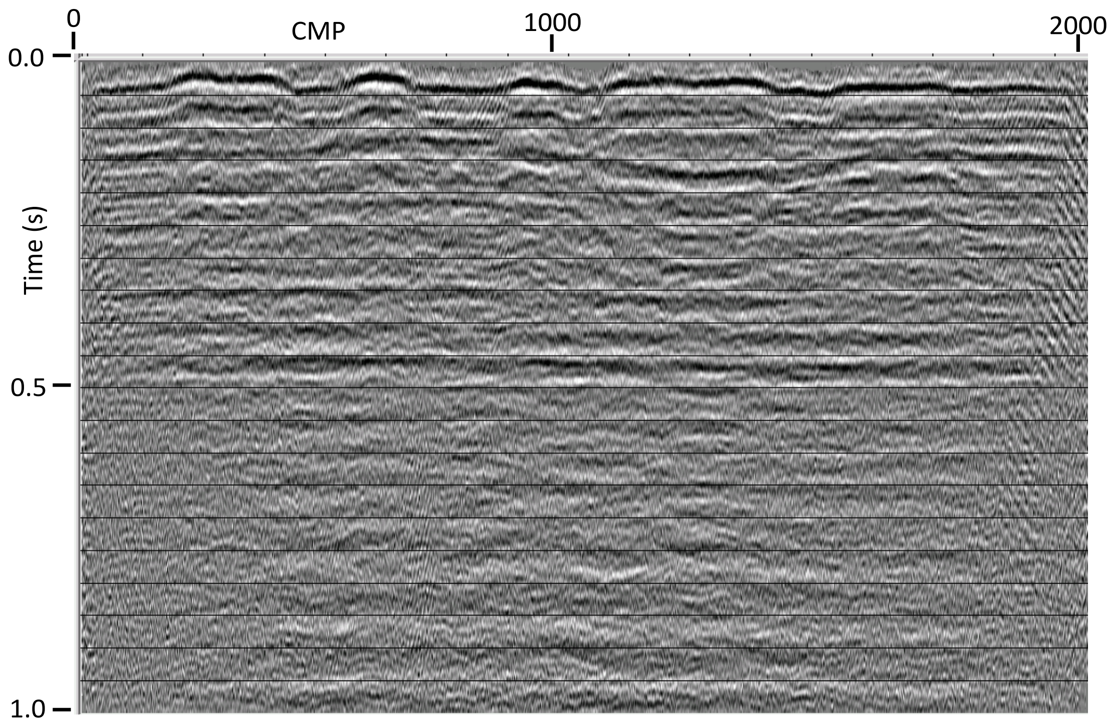

FIG.27. Stacked vertical component data from 'baseline' model in Figure 15, with random noise S/N = 1.0, after static correction by three passes of autostatics.

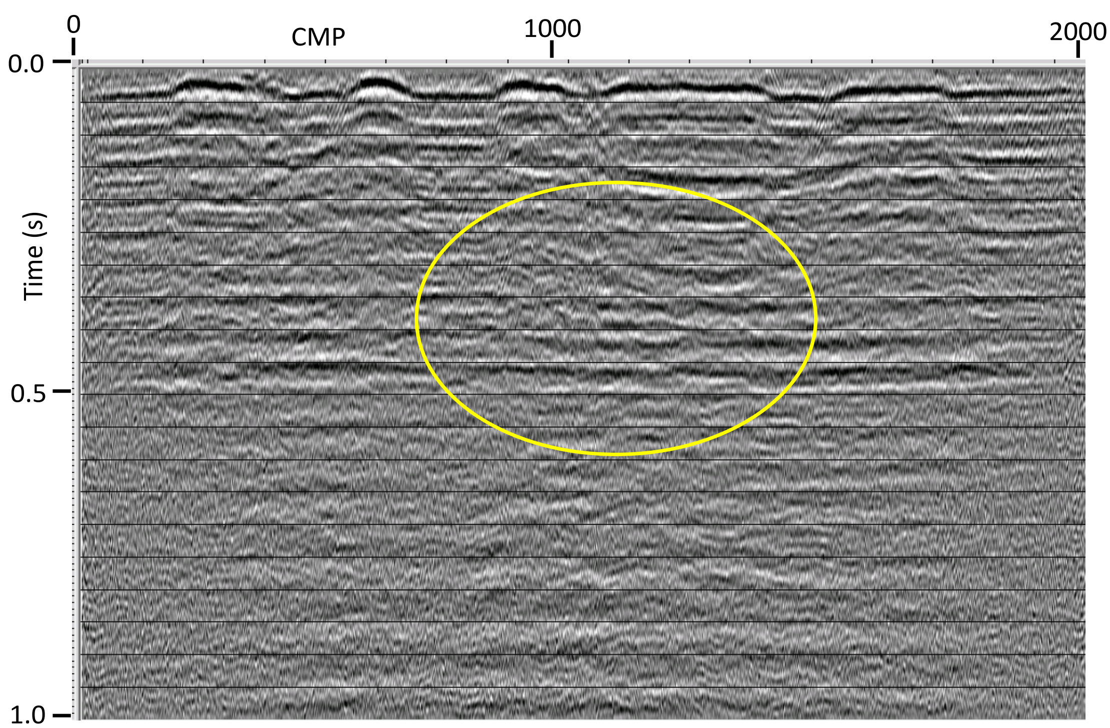

FIG.28. Stacked vertical component data from 'monitor' model in Figure 16, with random noise S/N = 1.0, after static correction by three passes of autostatics. The anomaly is barely visible when comparing with Figure 27.

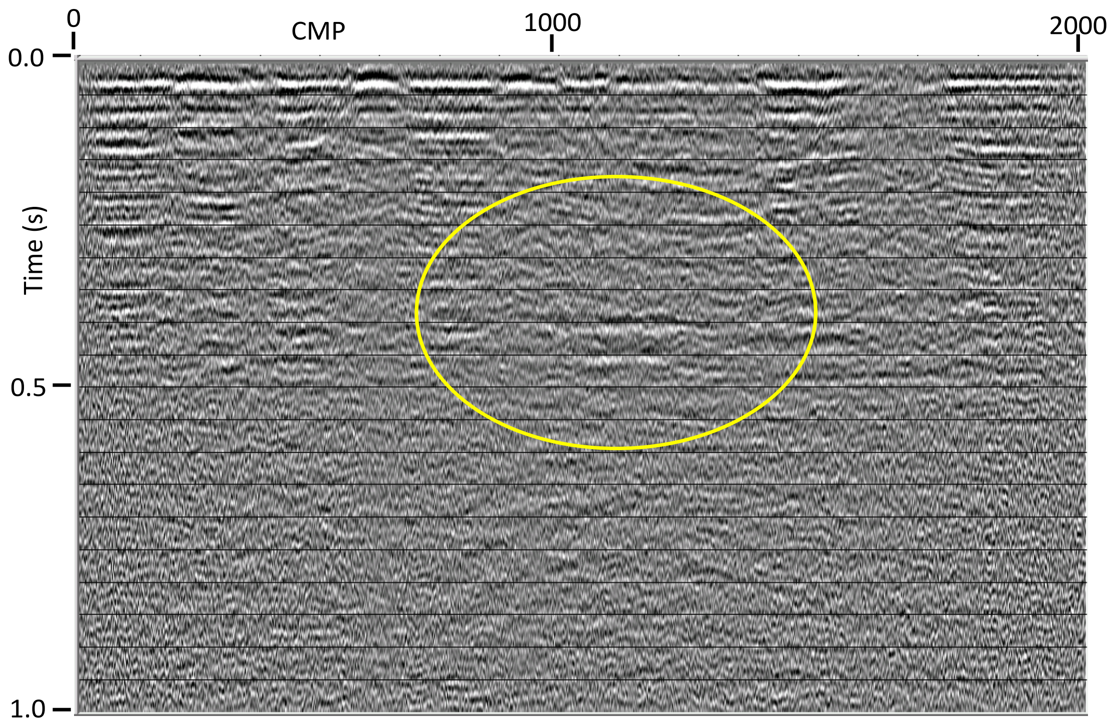

FIG.29. Difference between images in Figures 27 and 28. Although the anomaly is visible, it is weaker than the near-surface event, which is due to the 6ms time shift required to align the stack images to maximize the amplitude of the anomaly.

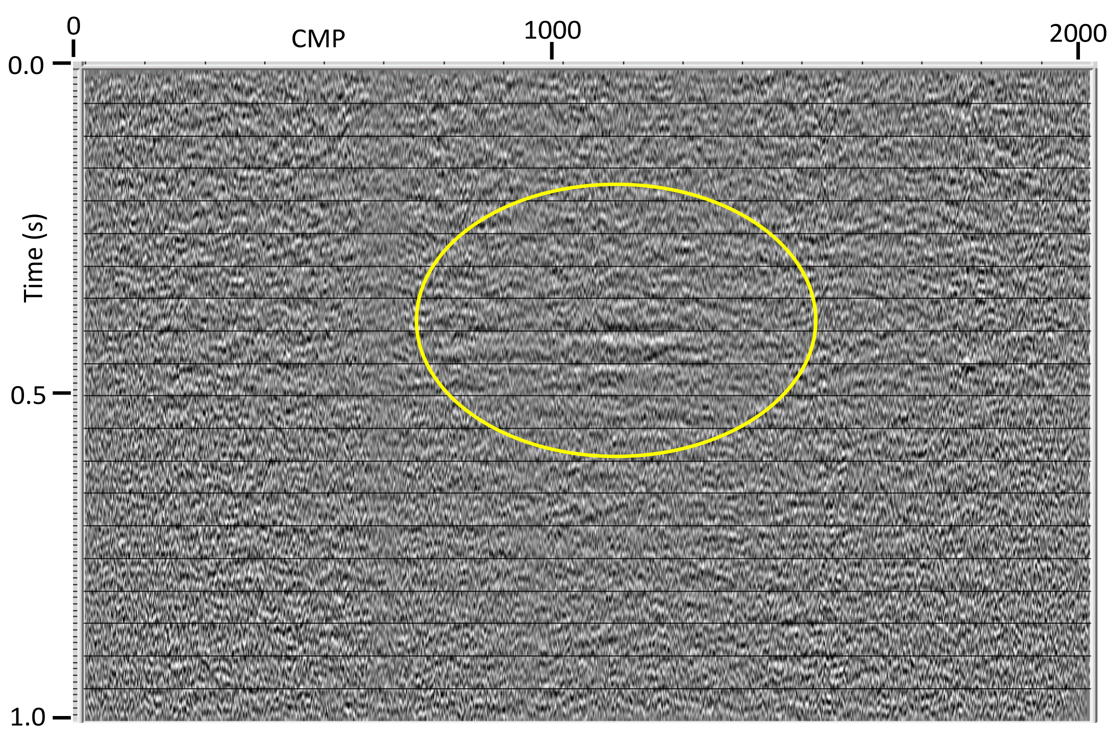

FIG.30. Difference between 'baseline' and 'monitor' images when the same autostatics solutions created for the 'baseline' model in Figure 27 are applied to the 'monitor' data as well.

A final complication added to the modeling experiment was the simulation of seasonal variations in the statics. The simulation was performed by picking a deliberately 'jittery' horizon across a source gather, then an unrelated 'jittery' horizon across a receiver gather. The jitters were done with hand-picking and were as random as possible, never exceeding approximately 10-15ms. The horizon picks were turned into surface-consistent statics simply by applying the de-biased source-gather horizon picks to each time-lapse vertical component source gather, then sorting the data to receiver gathers and applying the de-biased receiver-gather picks to each receiver gather, using the horizon-flattening module in ProMAX. In this case, because of these 'seasonal variations', we could not apply a statics solution from the baseline survey to the time-lapse survey—the autostatics needed to be computed independently for each survey. When this was done and the resulting static-corrected time-lapse stack and baseline stack were subtracted (after a relative bulk shift of 2ms), the result is shown in Figure 31. Perhaps surprisingly, the anomaly can still be seen, although not its top boundary. The fragments of higher amplitude along the top of the image probably reflect some of the differences in static solutions due to the simulated seasonal differences.

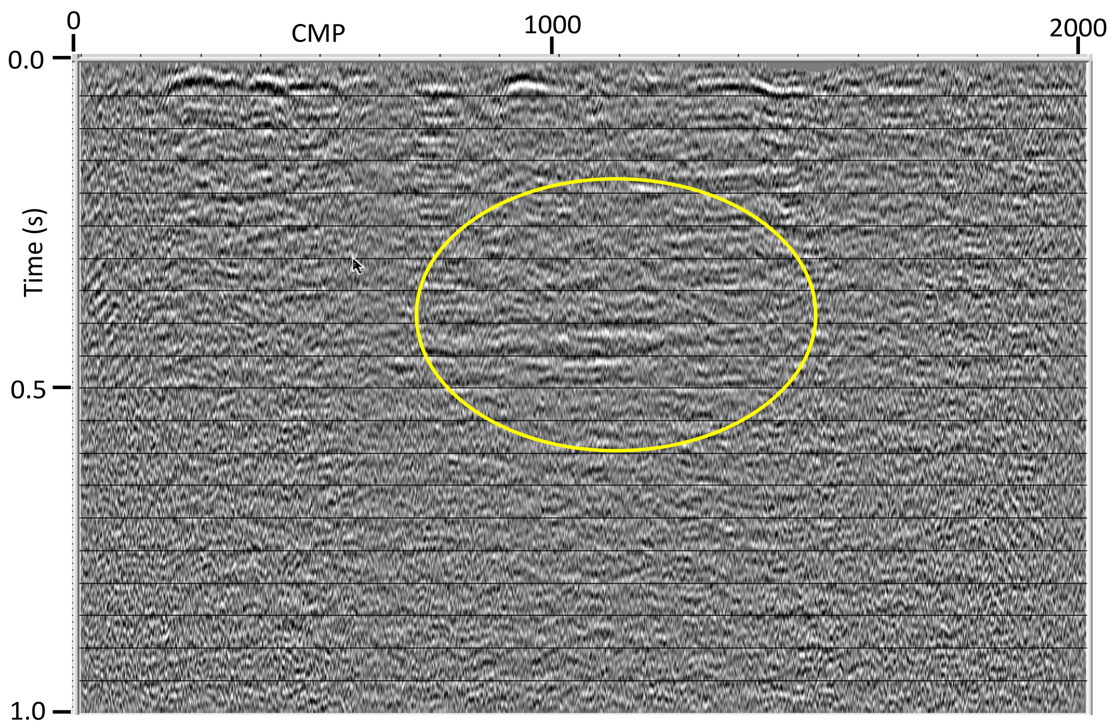

FIG.31. Difference image for 'baseline' vs. 'monitor' surveys when random statics due to 'seasonal differences' are modeled. The larger amplitudes at the surface are likely due to the actual differences in statics solutions between 'baseline' and 'monitor' surveys due to the simulated seasonal differences.

Raypath interferometry

Because of recent success with the use of raypath interferometry (Henley, 2012a) for applying static corrections to seismic field data (Henley, 2012b), we decided to try this method on the data from our time-lapse model study as well. Because there are no actual time shifts involved in raypath interferometry, properly registering the time-lapse stack against the baseline stack by applying a bulk time shift before subtraction is not necessary. Furthermore, by choosing the correlation gate and its weighting parameters, it is possible to focus the interferometry solution to favor various horizon levels. Figure 32 shows the interferometric solution for the random-noise-free baseline model (compare with Figure 22), while Figure 33 is the result for the random-noise-free time-lapse model (compare with Figure 23). In both these images, the reflection sequence between 350ms and 500ms is much stronger and more continuous than on the autostatics versions in Figures 22 and 23. On the other hand, because the interferometry procedure was concentrated on this reflection band, the undulating base-weathering reflection and details nearer the surface are less distinct. The difference between the images in Figures 32 and 33 is shown in Figure 34 (compare with Figure 24). On this figure, we see that the bottom of the time-lapse anomaly is very prominent, as are the time sag differences beneath it. The anomaly is much clearer here than on Figure 24, but it also has a greater lateral extent, a possible consequence of raypath interferometry.

We next applied raypath interferometry to the random-noise-contaminated baseline and time-lapse models. Surprisingly, as seen in Figures 35 and 36, the stack images are actually better than with the noise-free models. The stack difference image in Figure 37, however, shows that the noise does adversely affect the result. The anomaly is distinctly visible, but not nearly as strong as that from the noise-free models in Figure 34. Nevertheless, the bottom of the anomalous zone is well defined, and the time sag anomaly beneath is prominent, although not as widespread laterally. Furthermore, there are other regions on this stack difference image where obvious mismatches have occurred; but all are weaker than the actual anomalous zone. For a final comparison, we applied raypath interferometry to the time-lapse model with simulated seasonal statics, and re-computed the stack difference (Figure 38). In comparing this image with Figure 37, we see that the bottom event of the anomaly itself is weaker, but the time sag anomaly at 450ms becomes stronger.

Although not shown here, we repeated much of the above work for the surveys with simulated 10m receiver spacing. What we found was that the time-lapse anomaly was still detectable, whether we used autostatics or interferometry, but that the amplitude of the anomaly was much more laterally variable, and it was much harder to determine its edges. It seems that for data with lots of surface wave and random noise, or with significant statics, the lateral resolution and redundancy of the 2m receiver spread is necessary for unambiguous results.

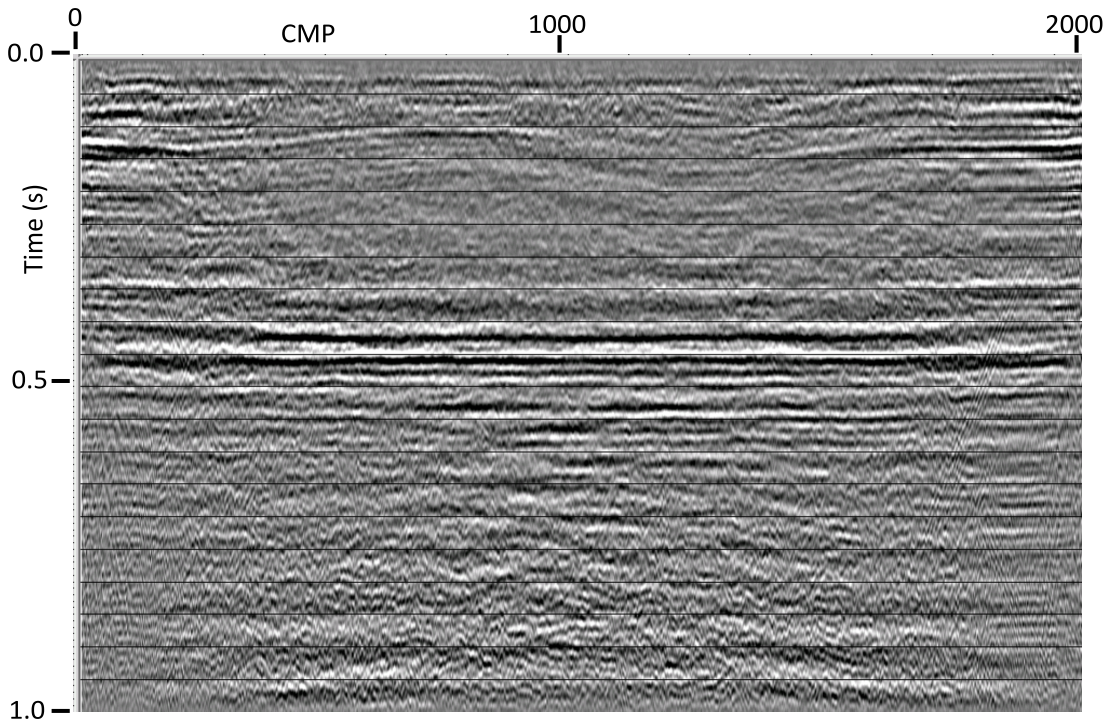

FIG.32. Stacked image of 'baseline' vertical component data after raypath interferometry for statics application. Events near the centre of the section are stronger because the windowing in the interferometric procedure focused the solution on these events.

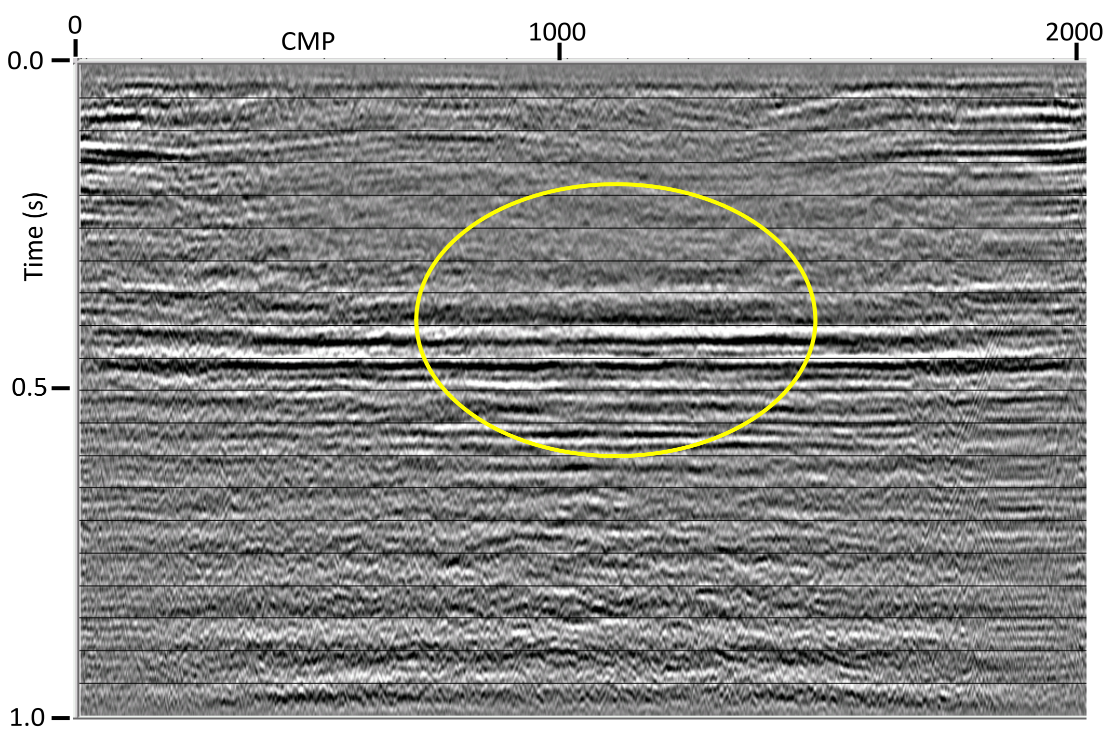

FIG.33. Stacked image of 'monitor' vertical component data after raypath interferometry to apply statics. The difference between the images in this figure and Figure 32 is only barely visible.

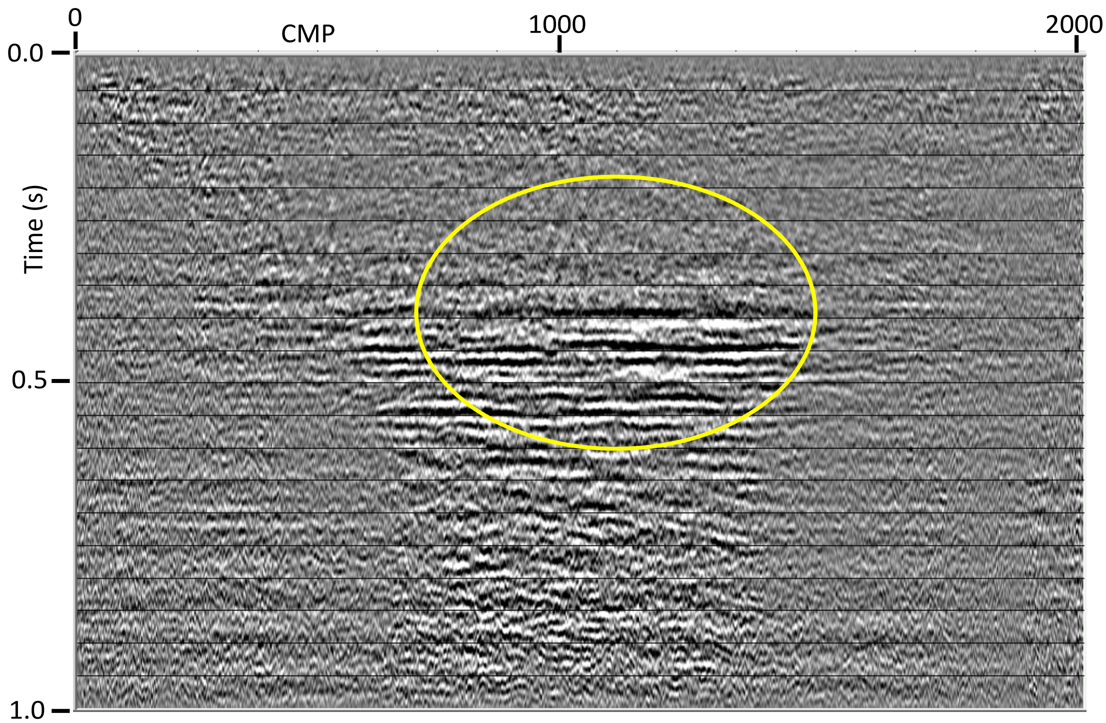

FIG.34. Difference between images in Figures 32 and 33. While the anomaly is very visible, its lateral extent is not well-resolved.

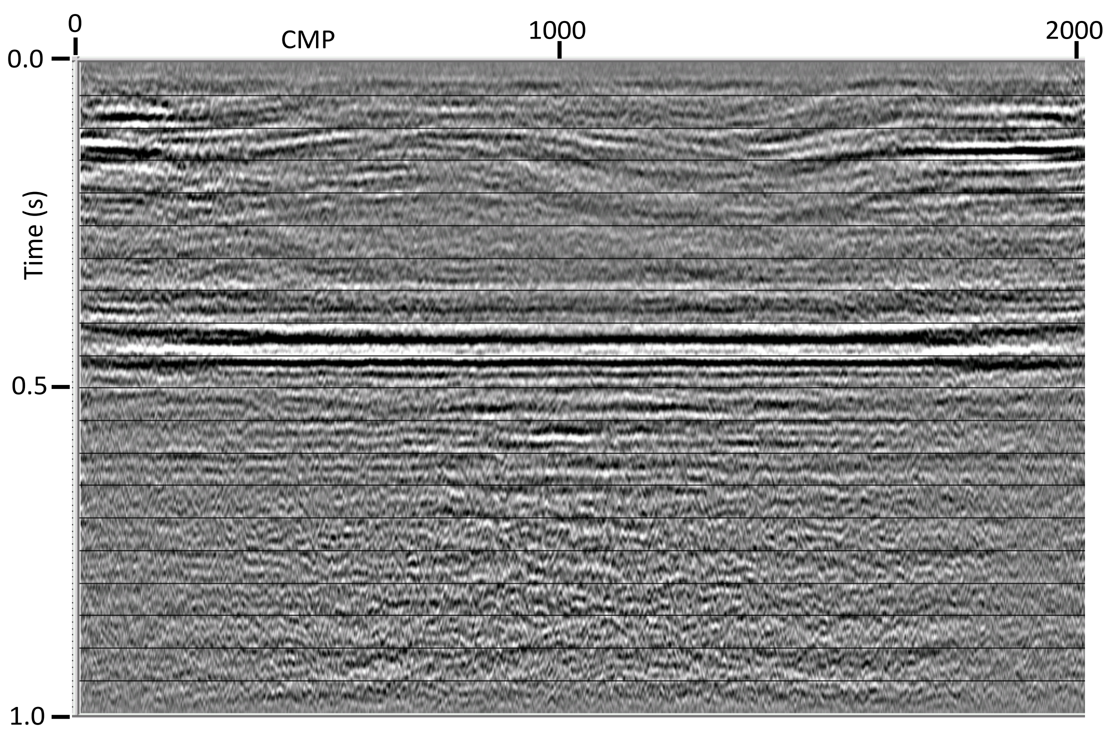

FIG.35. Stacked vertical component image for 'baseline' model with random noise S/N = 1.0, after raypath interferometry to apply static correction.

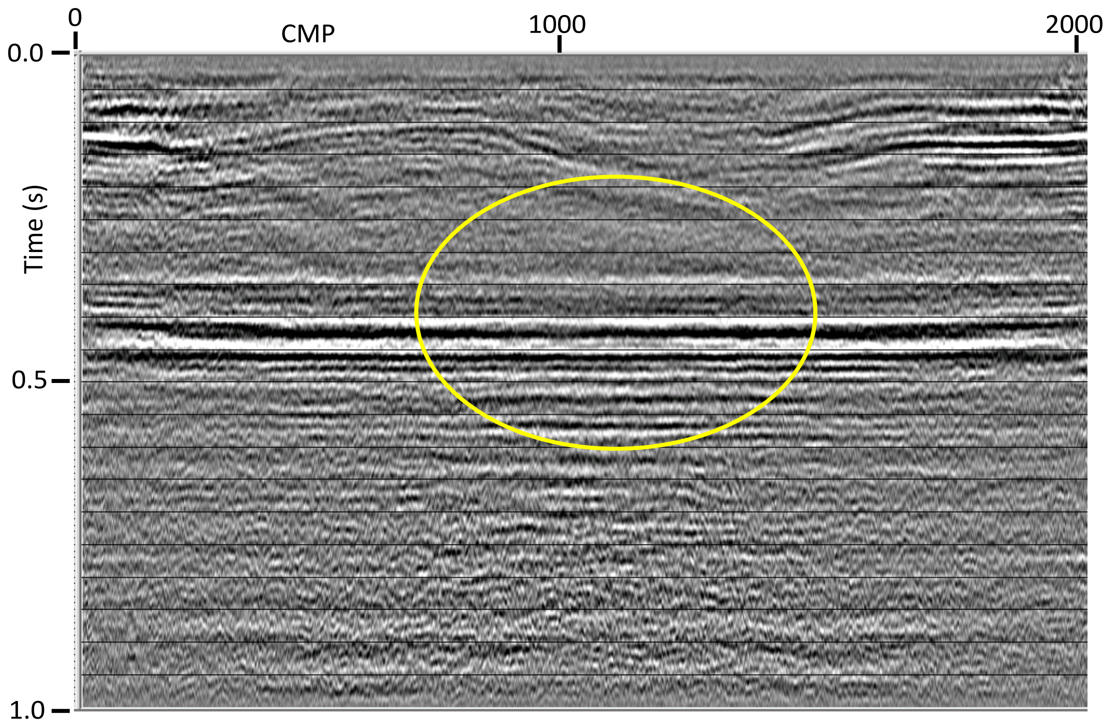

FIG.36. Stacked vertical component image for 'monitor' model with random noise S/N = 1.0, after raypath interferometry to apply static correction. Differences between this figure and Figure 35 are difficult to see.

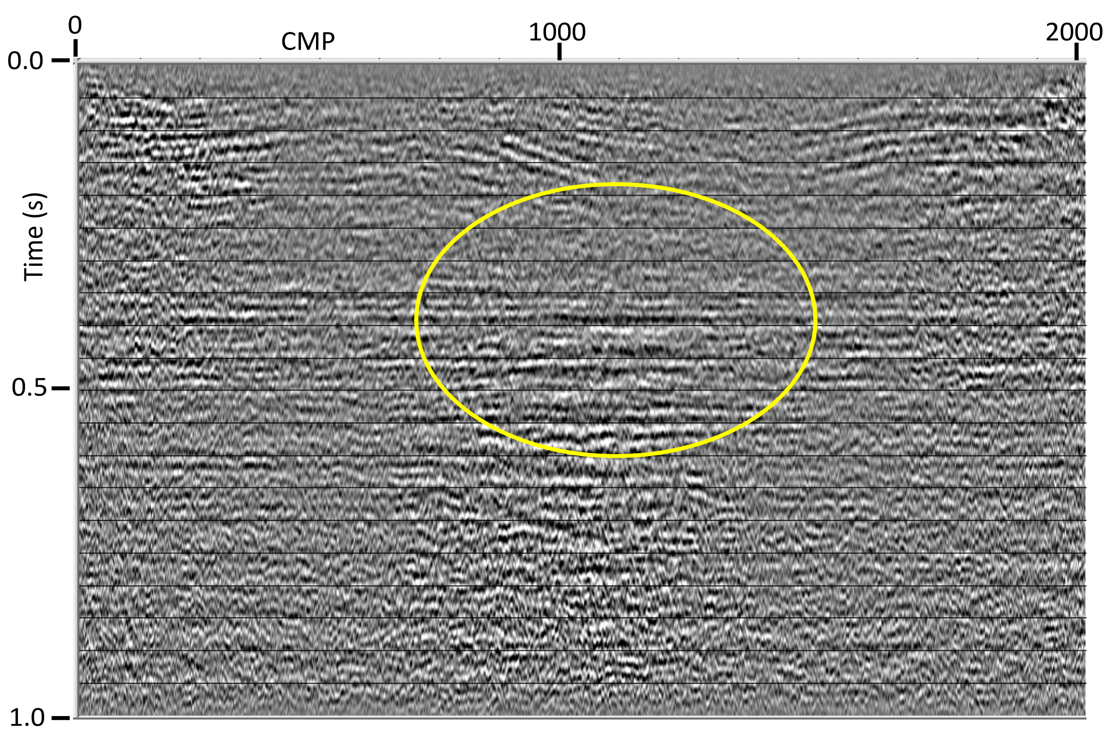

FIG.37. Difference between images in Figures 35 and 36. The anomaly is weaker than in Figure 34, but its lateral extent is more clearly represented.

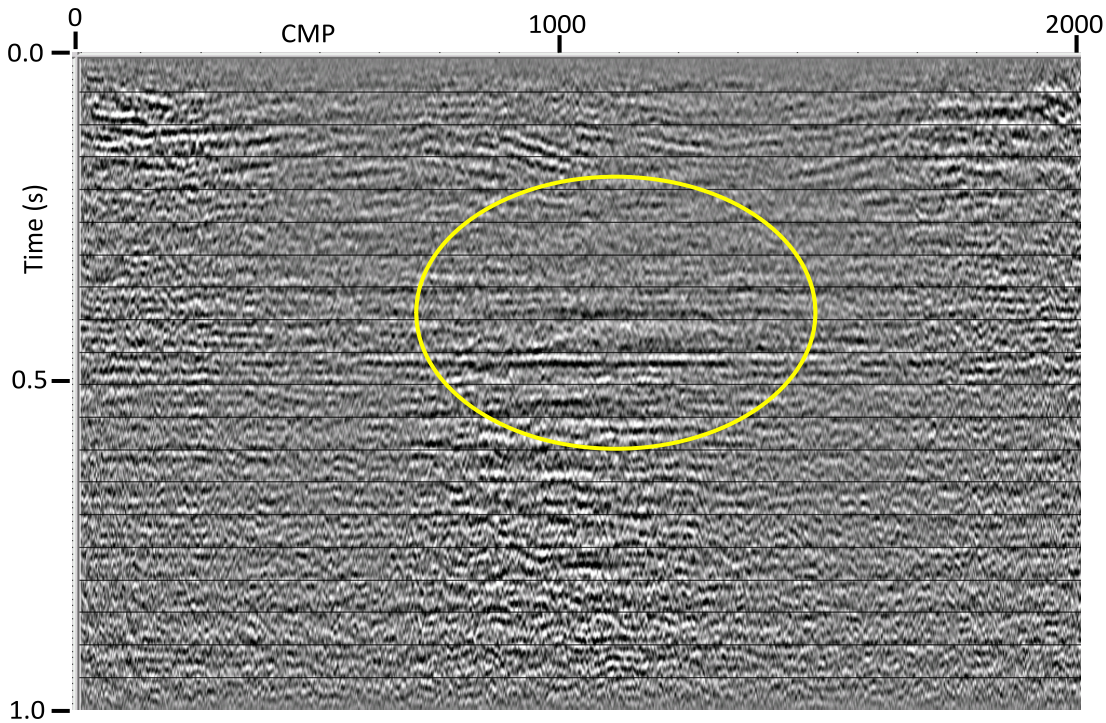

FIG.38. While the appearance of the anomaly has changed somewhat, its presence is still easily detected, in spite of simulated seasonal changes.

CONCLUSIONS

We have demonstrated the use of a 2D elastic wave modeling program to explore several survey repeatability issues key to the time-lapse technique for monitoring the progress of fluid production from a reservoir, or conversely, fluid injection into a formation. Using a relatively large, strong velocity anomaly, we showed that the detection of time-lapse differences is surprisingly robust under conditions of severe coherent and random noise contamination of the raw data, as long as the survey geometry remains the same for both baseline and time-lapse surveys, and as long as identical processing flows, with identical parameters, are used for both data sets. The presence of random noise influences the effectiveness of autostatics programs, so an anomaly is less detectable on data contaminated with large levels of random noise, unless the identical autostatics solution (from the baseline survey) is applied to both data sets.

Raypath interferometry can be used to provide the statics corrections, and is less sensitive to random noise; but time-lapse anomalies from interferometric stacks seem to be less well-resolved laterally. Simulated seasonal variations in surface conditions (seasonably variable statics) of modest magnitude do not greatly affect the detectability of the time-lapse anomaly, as long as the statics corrections, either autostatics or raypath interferometry, are applied independently to each data set. Finally, fine spatial sampling (2m receiver spacing, in this case) is not required on noise-free models with little near-surface detail; but when the near-surface supports strong surface waves and/or large statics, or there is strong random noise present, 2m resolution may be required to provide unambiguous difference results.

ACKNOWLEDGEMENTS

The authors acknowledge the support of CREWES sponsors and NSERC grant funds.

REFERENCES

Almutlaq, M.H., and Margrave, G.F., 2011, Application of surface-consistent matching filters (SCMF) on a time-lapse data set, 2911 CREWES research report, **23.**

Almutlaq, M.H. and Margrave, G.F., 2012, Time-lapse surface-consistent matching filters: two components versus four components, 2012 CREWES research report, **24.**

Almutlaq, M.H., and Margrave, G.F., 2012, Testing the surface-consistent matching filters algorithm on Violet Grove time-lapse data, 2012 CREWES research report, **24.**

Henley, D.C., 2011, Now you see it, now you don't: radial trace filtering tutorial, 2011 CREWES research report, **23.**

Henley, D.C., 2012a, Interferometric application of static corrections, Geophysics, **77,** No. 1, Q1-Q13.

Henley, D.C. 2012b, Interference and the art of static correction: raypath interferometry at Hussar, 2012 CREWES research report, **24.**

Manning, P. M., 2008, Techniques to enhance the accuracy and efficiency of finite-difference modelling for the propagation of elastic waves: PhD thesis, The University of Calgary.

Manning, P.M., 2009, Finite-difference staggered-grid modeling in 3 dimensions, 2009 CREWES research report, **21.**

Manning, P.M., 2010a, 2D finite-difference modeling in Matlab, version 1, 2010 CREWES research report, **22.**

Manning, P.M., 2010b,Correction filter use in finite-difference elastic modeling, 2010 CREWES research report,**22**.

Manning, P.M., 2011a, Comparisons between 2D and 3D finite-difference models of near source surface waves, 2011 CREWES research report, **23.**

Manning, P.M., 2011b, Numerical Rayleigh wave propagation on thin layers, 2011 CREWES research report, **23**.

Margrave, G.F., Lamoureux, M.P., and Henley, D.C., 2011, Gabor deconvolution: Estimating reflectivity by nonstationary deconvolution of seismic data, Geophysics, **76,** No. 3, pp W15-W30.

Ronen, J., and Claerbout, J.F., 1985, Surface-consistent residual statics estimation by stack-power maximization, Geophysics, **50,** 2759-2767.

Wong, J, Manning, P.M., and Henley, D.C., 2012, Elastic wave 2D modeling of seismic surveys, 2012 CREWES research report, **24.**